An efficient 3d/2d-covariant formulation of the spherical shallow water equations: well balanced DG approximation and application to tsunami and storm surge

Luca Arpaia, Mario Ricchiuto, Andrea Gilberto Filippini, Rodrigo Pedreros

To cite this version:

Luca Arpaia, Mario Ricchiuto, Andrea Gilberto Filippini, Rodrigo Pedreros. An efficient 3d/2d-covariant formulation of the spherical shallow water equations: well balanced DG approximation and application to tsunami and storm surge. 2021. hal-03207171

HAL Id: hal-03207171
https://brgm.hal.science/hal-03207171

Preprint submitted on 24 Apr 2021

An efficient 3d/2d-covariant formulation of the spherical shallow water equations: well balanced DG approximation and application to tsunami and storm surge

Luca Arpaia[1], Mario Ricchiuto[2], Andrea Gilberto Filippini[1] and Rodrigo Pedreros[1]

Coastal Risk and Climate Change, French Geological Survey
3 Av. C. Guillermin 45060 Orléans Cedex 2, France
and
Team Cardamom - INRIA, Univ. Bordeaux, CNRS, Bordeaux INP, IMB, UMR 5251,
200 Avenue de la Vieille Tour, 33405 Talence cedex, France

Abstract

In this work we consider an efficient discretization of the Shallow Water Equations in spherical geometry for oceanographic applications. Instead of classical 2d-covariant or 3d-Cartesian approaches, we focus on the mixed 3d/2d form of [Bernard et al., JCP 2009] which evolves the 2d momentum tangential to the sphere by projecting the 3d-Cartesian right-hand side on the sphere surface. First, by considering a covariant representation of the sphere instead of the finite element one, we show a simplification of the Discontinuous Galerkin scheme: local mass matrix goes back to the standard block-diagonal form, Riemann Problem do not imply tensor/vector rotation. Second we consider well-balancing corrections related to relevant equilibrium states for tsunami and storm surge simulations. These corrections are zero for the exact solution, and otherwise of the order of the quadrature formulas used. We show that their addition to the scheme is equivalent to resorting to the strong form the integral of the hydrostatic pressure term. The method proposed is validated on academic benchmarks involving both smooth and discontinuous solutions, and applied to realistic tsunami and an historical storm surge simulation.

Keywords: shallow water equations, spherical geometry, discontinuous galerkin, well-balanced schemes, tsunami, storm surge

---

1. Introduction

Coastal flooding is mainly caused by meteorological and telluric phenomena which may occur at the scale of the oceanic basin. The numerical simulation of such events requires to solve the governing equations

---

Email address: `l.arpaia@brgm.fr, mario.ricchiuto@inria.fr, a.filippini@brgm.fr, r.pedreros@brgm.fr` (Luca Arpaia[1], Mario Ricchiuto[2], Andrea Gilberto Filippini[1] and Rodrigo Pedreros[1])

Preprint submitted to *April 24, 2021*

in a spherical geometry. In this work we consider the Shallow Water Equations (SWEs) which provide satisfactory results for long wave phenomena such as tide/storm surge and tsunami.

The literature devoted to discrete formulation of the SWEs on the sphere is quite large. Two methods have emerged in the past to deal with the Earth curvature. A common approach among contemporary ocean models consists in a two-dimensional parametrization of the sphere through a proper curvilinear coordinate system. Then the primitive or shallow water equations are written directly on the curved manifold meaning that all the differential operators are transformed in curvilinear coordinates. A metric source term arises from the space variation of the curvilinear vectors basis. The underlying equations in curvilinear coordinates are typically discretized on regular grids with finite differences/finite volume schemes. Regional models uses the traditional latitude-longitude parametrization. Unfortunately for global ocean models, the latitude-longitude coordinate system has a singular point in the Arctic Ocean at the North Pole, where the meridians converge on water. The Jacobian of the coordinate transformation is not defined and moreover the singularity imposes a severe restriction on the maximum time step allowed for stability. Nowadays the pole problem is considered merely as an economical one [1]. In particular, meteorologists have used a variety of fixes to circumvent the singularity and all of such fixes employ multiple curvilinear coordinates defined on different patches covering the whole sphere, [2, 3]. Then a specific treatment of the flux term at the edges dividing the patches, where the tangent basis changes, is deployed: a rotation of momentum vector [4] or an orthonormalization of the Riemann Problem [5, 6] assure a common reference system at the edge and local conservation. To bypass the pole problem ocean modelers have used instead ad hoc curvilinear coordinates conceived to place the singularity point on lands, see for example the tripolar grid of [7]. Finally, for Finite Volume methods, some authors [6] claimed that extra care should be taken in the resolution of the Riemann Problem in curvilinear coordinates.

A second approach consists instead in resolving the governing PDEs in a three-dimensional Cartesian framework and then adding a constraint to force the currents to remain tangent to the sphere [8][9]. With this approach, it is more common to represent the sphere approximately through a local finite element map for each element. Thanks to the local map, no special treatment is required in polar regions to preserve accuracy and to conserve global mass.

A third approach seems to combine the advantages of both methods [10]: momentum time derivative is written with respect to 2d components while the right-hand side is first expressed in 3d and then projected back onto the sphere surface by a simple scalar product with respect to the tangent basis. The advantage is that the number of unknown is kept at a minimum (water depth and two momentum components) and, at the same time, the right-hand side mantains Cartesian form, thus it is independent from the parametrization of the sphere, and moreover there is no need to transform differential operators. For example, in tsunami applications this could be laborious for depth averaged non-hydrostatic models with dispersive terms that involve mixed high order derivatives. If requested, Riemann solvers are formulated easily in 3d Cartesian framework, and then projected on the sphere surface along with the right-hand side.

In [10], to threat the case of generic manifolds, the authors employed an approximate high order finite element representation of the geometry. Here we present some improvements of the original work of [10] applied to spherical geometry. First we use an exact representation of the sphere by means of a 2d covariant parametrization. This cancels the geometrical error related to the sphere curvature and the need of a high order representation of the spherical elements for a high order solution. We use the classical latitude longitude transformation for which simple expression of the transformation, covariant vector basis and their derivatives are available. Due to the orthogonality of covariant vector basis, the mass-matrix reduces to block diagonal form as in the plane case. Riemann solvers also simplify thanks to continuity of the sphere at the elements edges.

Second, within a Discontinuous Galerkin discretization (DG), we look to the discrete preservation of some steady states which are of particular interest for tsunami and storm surge computations. We show that the weak DG form (with one integration by parts) [11] is unable to preserve equilibria due to inexactness of quadrature formula with non-polynomial metric. As shown in [12], the so-called strong form (with double integration by parts) is more suited to retain general well-balanced states on the sphere. In this work we proceed in a slightly different manner and add well-balancing corrections related to relevant equilibrium states for tsunami and storm surge simulations. These corrections are zero for the exact solution and for exact integration, and otherwise of the order of the quadrature formulas used, at least when the solutions are smooth. We show that their addition to the scheme is equivalent to resorting to the strong form the integral of the hydrostatic pressure term.

The paper is organized as follows. In section 2 we introduce the notation for the spherical geometry. In section 3 we introduce the SWEs in the 3d-2d covariant formulation. In section 4 we discuss their Well-Balanced DG approximation. In section 5 we details computational aspects such as pole treatement and shock-capturing. In section 6 we evaluate the proposed methods on standard global benchmarks for the shallow water equations on the sphere and on regional realistic tsunami/storm surge computations.

2. Spherical map

We consider a sphere $\mathcal{S}^2$ with radius R described by curvilinear coordinates $\{X^1, X^2\}$ and orthogonal but not orthonormal covariant basis $\{\boldsymbol{g}_1, \boldsymbol{g}_2\}$. The coordinate vector $\boldsymbol{x}$ then writes:

$$\begin{aligned} \boldsymbol{x} &= x^i \boldsymbol{e}_i \equiv x^1 \boldsymbol{e}_1 + x^2 \boldsymbol{e}_2 + x^3 \boldsymbol{e}_3 \qquad (1) \\ &= X^\alpha \boldsymbol{g}_\alpha \equiv X^1 \boldsymbol{g}_1 + X^2 \boldsymbol{g}_2 \qquad (2) \end{aligned}$$

Note that in the above definitions and in the following repeated indices imply summation. In particular, Latin indices are used for the components of vectors in Cartesian coordinates (from 1 to 3), while Greek indices are used for vectors in local curvilinear coordinates (from 1 to 2). The spherical transformation $\boldsymbol{x} = G(\boldsymbol{X})$ has an inverse $\boldsymbol{X} = G^{-1}(\boldsymbol{x})$, a Jacobian or transformation tensor:

$$\boldsymbol{J}_G = \frac{\partial \boldsymbol{x}}{\partial \boldsymbol{X}} \qquad (3)$$

with components $J_G^{i\alpha}$ and an inverse Jacobian:

$$\boldsymbol{J}_G^{-1} = \frac{\partial \boldsymbol{X}}{\partial \boldsymbol{x}} \qquad (4)$$

with components $(J_G^{-1})^{\alpha i}$. The covariant vectors define the tangent plane to the sphere. They can be obtained by differentiation as the columns of the Jacobian $\boldsymbol{g}_i = \frac{\partial \boldsymbol{x}}{\partial X^i}$. It is useful to normalize the basis:

$$\boldsymbol{g}_i^* = \frac{\boldsymbol{g}_i}{||\boldsymbol{g}_i||} \qquad (5)$$

in order that $\boldsymbol{g}_i^* \cdot \boldsymbol{g}_j^* = \delta_{ij}$.

Although $\{X^1, X^2\}$ could be any available parametrization of the sphere, in this work we have used a latitude-longitude parametrization, thus for us, X_1 will be the longitude and X_2 the latitude. This allows to evolve momentum directly in physical relevant quantities (northward and eastward components). As already mentioned, this introduce a singularity that will be discussed in section 4.1.

3. Shallow Water Equations in spherical geometry

We consider the SWEs in spherical geometry with uneven bathymetry and in presence of earth rotation. We express them in a generic vector form:

$$\begin{aligned} \frac{\partial h}{\partial t} + \nabla \cdot h\boldsymbol{u} &= 0 \qquad (6) \\ \frac{\partial h\boldsymbol{u}}{\partial t} + \nabla \cdot \boldsymbol{T} &= \boldsymbol{S} \qquad (7) \end{aligned}$$

with h the fluid depth, $h\boldsymbol{u}$ the discharge/momentum vector, and having denoted the momentum flux tensor by $\boldsymbol{T}$. The source $\boldsymbol{S}$ includes the effects of bathymetry, Coriolis force, and meteorological forcing:

$$\boldsymbol{S} = gh\nabla b + \Omega\boldsymbol{k} \times h\boldsymbol{u} + \frac{gh}{\rho_0}\nabla p_{atm} + f_{\mathrm{w}} \tag{8}$$

The the formula above $b(\boldsymbol{x})$ denoted the bathymetry/topography, Ω the Earth rotation rate and $\boldsymbol{k}$ the Earth rotation axis. p_{atm} is the atmospheric pressure, ρ_0 is the water density and f_{w} represents wind forcing. The expression for nabla $\nabla\cdot$, vector $h\boldsymbol{u}$ and tensor $\boldsymbol{T}$ depends on the coordinate system in which they are expressed. As mentioned in the introduction, the most common representations used for the shallow water equations are wither 3d Cartesian coordinates or curvilinear coordinates. The momentum vector $h\boldsymbol{u}$ can be expressed in both systems as:

$$\begin{aligned} h\boldsymbol{u} &= hu^i\boldsymbol{e}_i \equiv hu^1\boldsymbol{e}_1 + hu^2\boldsymbol{e}_2 + hu^3\boldsymbol{e}_3 && (9) \\ &= hu^\alpha\boldsymbol{g}_\alpha \equiv hu^{\alpha_1}\boldsymbol{g}_1 + hu^{\alpha_2}\boldsymbol{g}_2 && (10) \end{aligned}$$

We remark that, for curvilinear coordinates, momentum components are not defined in a unitary basis. It may be convenient expressing momentum in a unitary basis:

$$\begin{aligned} h\boldsymbol{u} &= hu^\alpha||\boldsymbol{g}_\alpha||\frac{\boldsymbol{g}_\alpha}{||\boldsymbol{g}_\alpha||} && (11) \\ &= hu^{*\alpha}\boldsymbol{g}^*_\alpha && (12) \end{aligned}$$

The relationship between the velocity components written in the two basis is:

$$u^i = J_G^{i\alpha}u^\alpha, \quad u^i = J_G^{*,i\alpha}u^{*\alpha} \tag{13}$$

where $J_G^{*,i\alpha} = J_G^{i\alpha}/||\boldsymbol{g}_\alpha||$ (standard summation does not apply here) is the Jacobian (3) normalized by columns. Similarly the second order flux tensor $\boldsymbol{T}$ can be expressed in both coordinate systems as:

$$\begin{aligned} \boldsymbol{T} &= T^{ij}\boldsymbol{e}_i\boldsymbol{e}_j && (14) \\ &= T^{\alpha\beta}\boldsymbol{g}_\alpha\boldsymbol{g}_\beta && (15) \end{aligned}$$

with Cartesian components $T^{ij} = huu^{ij} + P\delta_{ij}$ and curvilinear components $T^{\alpha\beta} = huu^{\alpha\beta} + GP$. The hydrostatic pressure is defined as $P = gh^2/2$, and G is the determinant of the metric tensor constructed from the Jacobian matrix as $\boldsymbol{G} = \boldsymbol{J}_G^T\boldsymbol{J}_G$.

3.1. Equilibrium states

For coastal flows, an important role is played by the so-called *lake at rest* state which, denoting the free surface level $\eta = h + b$, is the particular steady solution characterized by the two invariants [13]:

$$h\boldsymbol{u} = 0, \quad K = \eta = const = K_0 \tag{16}$$

In presence of atmospheric pressure forcing, a relevant state is the *inverted barometer* balance that is an exact solution of the SWEs in case of full adjustment of sea level to changes in barometric pressure [14]:

$$h\boldsymbol{u} \quad = 0, \quad K = \eta + \tfrac{p_{atm}}{g\rho_0} = const = K_1 \tag{17}$$

Full adjustment is never reached since the pressure field is unsteady $p_{atm}(\boldsymbol{x}, t)$, thus one may question if this is really a relevant equilibrium, but it is interesting to be able to handle this possibility numerically. In [15] they showed that, at least in deep water, the free surface response is almost isostatic and characterized by small perturbations around the inverted barometer balance. In light of these findings and for completeness, we have investigated the more general balance (17).

A numerical method approximating (6)(7) is said to be Well-Balanced if (16) or (17) are also exact solutions of the discrete equations. In other words, Well-balanced schemes provide a discrete analog of the balance between hydrostatic pressure and the forces exerted by the bottom (and by atmospheric pressure)

$$\nabla \cdot P\boldsymbol{I} = -gh\nabla\left(b + \frac{p_{atm}}{g\rho_0}\right) \tag{18}$$

3.2. Fully diagonal mixed 3d/2d-covariant formulation

We present a modified 3d/2d form of the original [10] with a 2d-covariant parametrization. We project momentum equation (7), with the right-hand side expressed in 3d Cartesian framework, on the tangent plane. We have seen that, for the sphere, simple analytical expressions exist for the for tangent vector basis $\boldsymbol{g}_\alpha = \frac{\partial \boldsymbol{x}}{\partial X^\alpha}$. It is better to project onto the normalized tangent basis (5):

$$\frac{\partial}{\partial t}(h\boldsymbol{u} \cdot \boldsymbol{g}^*_\alpha) + (\nabla \cdot \boldsymbol{T}) \cdot \boldsymbol{g}^*_\alpha \quad = \quad \boldsymbol{S} \cdot \boldsymbol{g}^*_\alpha \tag{19}$$

or by components α:

$$\begin{aligned}
& && \frac{\partial}{\partial t}(hu^{*\alpha}) + \frac{\partial T^{jk}}{\partial x^k} g^{*j}_\alpha = S^j g^{*j}_\alpha \\
&\text{e.g.} \quad (\alpha = 1) && \frac{\partial}{\partial t}(hu^1 \underbrace{\boldsymbol{g}^*_1 \cdot \boldsymbol{g}^*_1}_{=1} + hu^2 \underbrace{\boldsymbol{g}^*_2 \cdot \boldsymbol{g}^*_1}_{=0}) + \left(\frac{\partial T^{11}}{\partial x^1} + \frac{\partial T^{12}}{\partial x^2} + \frac{\partial T^{13}}{\partial x^3}\right) g^{*1}_1 \\
& && \qquad + \left(\frac{\partial T^{21}}{\partial x^1} + \frac{\partial T^{22}}{\partial x^2} + \frac{\partial T^{23}}{\partial x^3}\right) g^{*2}_1 \\
& && \qquad + \left(\frac{\partial T^{31}}{\partial x^1} + \frac{\partial T^{32}}{\partial x^2} + \frac{\partial T^{33}}{\partial x^3}\right) g^{*3}_1 = S^j g^{*j}_1
\end{aligned}$$

One advantage of this formulation with respect to full 3d equations is that the number of unknowns is kept minimum (h, hu^1, hu^2). Another attractive feature is that the flux function is in 3d form and does not depend on a particular transformation. This means that line integrals are defined intrinsically and mass/momentum is easily conserved circumventing implementation issue related to the use of composite meshes in the 2d approach. The drawback is complexity: for each momentum equation 9 components of the fluxes has to be evaluated instead of three. Compared to [10] the main difference here is that we will not project the sphere onto a finite element approximation, but use the exact parametrization as well as use the exact covariant basis also in the finite element discretization. This allows to take advantage of the orthogonality of the covariant basis and work with a fully diagonal system.

4. Well balanced discontinuous finite element discretization

We consider a discretization of $\mathcal{S}^2$ composed by non overlapping triangular elements $\mathcal{K}$. To each element $\mathcal{K}$ we can associate an element defined in the parametric space, which we denote by K. For a given mesh, we label by the roman h the characteristic mesh size measured in physical space. Following a high order DG Galerkin procedure, we project the vector of conserved variables and the bathymetry into the finite dimensional space:

$$V_{\mathrm{h}}^p = \{\varphi : \varphi(\boldsymbol{x}) \in L_K^p, \boldsymbol{x} \in K\} \tag{20}$$

where L_K^p are Lagrange polynomials of degree p defined on each parametric element K. We obtain the weak formulation multiplying (19) by a smooth test function φ_i that belongs to the same space (20) and integrating it on a spherical triangle $\mathcal{K}$:

$$\frac{\partial}{\partial t}\int_{\mathcal{K}} h\boldsymbol{u}_{\mathrm{h}} \cdot \boldsymbol{g}_\alpha^* \varphi_i \, d\boldsymbol{x} + \int_{\partial\mathcal{K}} \boldsymbol{T}_{\mathrm{h}}^{\curlyvee} \boldsymbol{g}_\alpha^* \varphi_i \cdot \boldsymbol{n} \, ds - \int_{\mathcal{K}} \boldsymbol{T}_{\mathrm{h}} : \nabla\left(\boldsymbol{g}_\alpha^* \varphi_i\right) \, d\boldsymbol{x} = \int_{\mathcal{K}} \boldsymbol{S}_{\mathrm{h}} \cdot \boldsymbol{g}_\alpha^* \varphi_i \, d\boldsymbol{x} \tag{21}$$

As noted in [10], if we regroup $\boldsymbol{g}_\alpha^* \varphi_i = \boldsymbol{v}_\alpha$, then (21) corresponds to consider a vectorial test function for each momentum equation. $\boldsymbol{T}_{\mathrm{h}}^{\curlyvee}$ denotes the numerical flux evaluated at the elements boundaries. The symbol : is the scalar product between second order tensors $\boldsymbol{A} : \boldsymbol{B} = A_{ij}B_{ji}$.

Several aspects need to be clarified. First of all the mapping required to define the quadrature formulas, which will involve non-algebraic transformations. Secondly, the well-balancedness w.r.t the equilibria presented earlier is not trivial in this formulation as exact quadrature is impossible due to the mapping adopted. These aspects are covered in the next sections.

4.1. Reference element mapping for quadrature

In practice all the integrals are computed on the standard reference triangle K_0. The transformation which map a reference triangle to a spherical triangle is denoted by

$$A : K_0 \to \mathcal{K}, \quad \boldsymbol{x} = A(\boldsymbol{X}_0) \tag{22}$$

with Jacobian

$$\boldsymbol{J}_A = \frac{\partial \boldsymbol{x}}{\partial \boldsymbol{X}_0}, \quad J_A = \det \boldsymbol{J}_A \tag{23}$$

Differently form [10] we do not employ a finite element approximation for A. Instead we keep an exact geometrical representation of the sphere by expressing A as:

$$\begin{aligned} \boldsymbol{x} &= \frac{R}{\|\sum_{j=1}^{N_{Dofs}} \varphi_j(\boldsymbol{X}_0)\boldsymbol{x}_j\|} \sum_{j=1}^{N_{Dofs}} \varphi_j(\boldsymbol{X}_0)\boldsymbol{x}_j \\ &:= R\frac{F(\boldsymbol{X}_0)}{\|F(\boldsymbol{X}_0)\|} \end{aligned}$$

where F is the P1 finite element transformation from the reference element to the 3d element. The above transformation has a smooth Jacobian everywhere which can be computed as:

$$\frac{\partial x^k}{\partial X_0^\beta} = \frac{R}{\|F\|} \sum_{j=1}^{N_{Dofs}} \frac{\partial \varphi_j}{\partial X_0^\beta} x_j^k - \frac{R\sum_{j=1}^{N_{Dofs}} \varphi_j(\boldsymbol{X}_0)x_j^k}{\|F\|^2} \frac{\partial \|F\|}{\partial X_0^\beta}$$

Then the gradient operator can be transformed with respect to the reference curvilinear coordinates:

$$\frac{\partial}{\partial x^k} = \frac{\partial}{\partial X_0^\beta}\frac{\partial X_0^\beta}{\partial x^k} = \frac{\partial}{\partial X_0^\beta}(J_A^{-1})^{\beta k}$$

where the inverse Jacobian of the transformation is intended as the pseudo-inverse $\boldsymbol{J}_A^{-1} = \boldsymbol{G}_A^{-1}\boldsymbol{J}_A^T$ with $\boldsymbol{G} = \boldsymbol{J}_A^T\boldsymbol{J}_A$ the metric tensor.

For the evaluation of the surface integrals we need the transformation of the area differential:

$$d\boldsymbol{x} = J_A \, d\boldsymbol{X}_0$$

the determinant of the Jacobian is computed through the metric tensor determinant $J_A = \sqrt{\det \boldsymbol{G}}$.

Finally the variation of the tangent basis can be also expressed in a form which is easy to compute. In fact using chain rule and the definition (4):

$$\frac{\partial g_\alpha^{*j}}{\partial x^k} = \frac{\partial g_\alpha^{*j}}{\partial X^\beta}\frac{\partial X^\beta}{\partial x^k} = \frac{\partial g_\alpha^{*j}}{\partial X^\beta}(J_G^{-1})^{\beta k} \tag{24}$$

where we have to compute vector basis derivatives $\frac{\partial g_\alpha^{*j}}{\partial X^\beta}$ (for the sphere it's easy). All these relationships can be plugged in (26)(25) and then integrals are performed by quadrature on the reference element K_0. For example the momentum flux integral becomes

$$\begin{aligned} \int_{\mathcal{K}} \boldsymbol{T}_{\mathrm{h}} : \nabla\left(\boldsymbol{g}_\alpha^* \varphi_i\right) \, d\boldsymbol{x} &= \int_{\mathcal{K}} T_{\mathrm{h}}^{kj} \frac{\partial}{\partial x^k}\left(g_\alpha^{*j}\varphi_i\right) \, d\boldsymbol{x} \\ &= \int_{\mathcal{K}} T_{\mathrm{h}}^{kj} \varphi_i \frac{\partial g_\alpha^{*j}}{\partial x^k} \, d\boldsymbol{x} + \int_{\mathcal{K}} T_{\mathrm{h}}^{kj} g_\alpha^{*j} \frac{\partial \varphi_i}{\partial x^k} \, d\boldsymbol{x} \qquad (25) \end{aligned}$$

The first term is the standard DG volume term. A second term, related to the space variation of the tangent covariant vectors, appears and it closely resembles the metric source term of the curvilinear 2d approach [16]. More interestingly, the time derivative term can be written as

$$\frac{\partial}{\partial t}\int_{\mathcal{K}} h\boldsymbol{u}_{\mathrm{h}}\cdot\boldsymbol{g}^{*}_{\alpha}\varphi_i\,d\boldsymbol{x} = \sum_{j\in DOFs}\int_{\mathcal{K}}\varphi_i\varphi_j\,d\boldsymbol{x}\,\frac{\partial hu^{*\alpha}_j}{\partial t} \tag{26}$$

Since time derivative in momentum equation is uncoupled, differently from [10] the mass matrix remains block-diagonal which is the main advantage of the formulation proposed here. Please note also that this algorithm evolves physical components of momentum $hu^{*\alpha}$ (in m^2/s eastward ($\alpha = 1$) and northward $\alpha = 2$) at the degrees of freedom.

Differently from two-dimensional formulations, the right-hand side appears in Cartesian form and it is well-posed on the whole sphere. However the tangent basis in (21) is not well defined at the poles, for the latitude-longitude parametrization that we have chosen. For this reason, only to evaluate the tangent basis and its derivatives, a polar cap defined by a limiting latitude z_{lim}, is deployed. Elements are flagged according to the baricenter position: if $z_G^K > z_{\mathrm{lim}}$ we use a rotated spherical transformation replacing $(x^1, x^2, x^3) \to (x^1, x^3, -x^2)$ in (1). Jacobian (3), inverse Jacobian (4) and basis vectors (5) are modified accordingly. We found that the DG framework is well suited to handle such discontinuity at the elements edges since no communication between elements is needed, which in turn means that no modification must be done to the algorithm. In particular:

- each element updates the momentum components $hu^{*\alpha}$ in its own reference system, thus zonal/meridional components in standard elements and rotated components in polar cap elements.
- in a DG method, communication between elements is needed only for evaluating numerical fluxes. Since they are computed in a 3d framework (and independent from the local coordinate system) no specific treatment is necessary at the edges separating the polar cap.

In practice we have set $z_{lim} = 0.9R$, however this value has no impact on the numerical results.

4.2. Well balanced correction and relation with inexact quadrature

We study now the well-balanced nature of the scheme. We will first consider the lake at rest case. The effect of the atmospheric pressure is added introducing an apparent topography [17] $b \to B = b + \frac{p_{atm}}{g\rho_0}$. Imposing the lake at rest, the momentum components of the DG method reduce to:

$$\int_{\partial\mathcal{K}} P_{\mathrm{h}}^{\curlyvee}\boldsymbol{I}\boldsymbol{g}^{*}_{\alpha}\varphi_i\cdot\boldsymbol{n}\,ds - \int_{\mathcal{K}} P_{\mathrm{h}}\boldsymbol{I} : \nabla\left(\boldsymbol{g}^{*}_{\alpha}\varphi_i\right)\,d\boldsymbol{x} = -\int_{\mathcal{K}} gh_{\mathrm{h}}\nabla b\cdot\boldsymbol{g}^{*}_{\alpha}\varphi_i\,d\boldsymbol{x} \tag{27}$$

One drawback of the mixed formulation emerges: well-balancing is lost because of the projection on the tangent basis, an operation that involves the evaluation of non-algebraic functions in all of the three integrals of (27). Indeed even with constant bathymetry, and constant pressure, in general we cannot remove the geometrical integration error

$$\epsilon^K_{P_0} = P_0 \left[\int_{\mathcal{K}} \boldsymbol{I} : \nabla \left(\boldsymbol{g}^*_\alpha \varphi_i \right) \, d\boldsymbol{x} - \int_{\partial\mathcal{K}} \boldsymbol{I} \boldsymbol{g}^*_\alpha \varphi_i \cdot \boldsymbol{n} \, ds \right] \tag{28}$$

This is an issue already encoutered on curved finite element (polynomial) meshes [18], and is even more critical for the non-polynomial approximation used here. We remark that this was also highlighted in [12] when in the context of the study of the well-balancing of a fully 3d DG shallow water approximation on the sphere. As observed in the last reference, a more suitable form to guarantee the well -balanced character of the method is the strong form. We obtain a similar result here, but we proceed in a different manner, and only focus on the pressure, the convective part of the flux playing no role for the equilibria we are interested in.

Essentially, our idea is to explicitly re-inject into the scheme the integration by part error

$$\epsilon^K_P = \int_{\mathcal{K}} P_{\mathrm{h}} \boldsymbol{I} : \nabla \left(\boldsymbol{g}^*_\alpha \varphi_i \right) \, d\boldsymbol{x} - \int_{\partial\mathcal{K}} P_{\mathrm{h}} \boldsymbol{I} \boldsymbol{g}^*_\alpha \varphi_i \cdot \boldsymbol{n} \, ds + \int_{\mathcal{K}} \left(\nabla \cdot P_{\mathrm{h}} \boldsymbol{I} \right) \cdot \boldsymbol{g}^*_\alpha \varphi_i \, d\boldsymbol{x} \tag{29}$$

which of course reduced to (28) if the pressure is constant. The above term can be trivially shown to be bounded by the maximum between the approximation error and the quadrature error, thus within the truncation of the scheme. The variational form used in practice is thus given by

$$\begin{aligned} \frac{\partial}{\partial t} \int_{\mathcal{K}} h_{\mathrm{h}} \varphi_i \, d\boldsymbol{x} + \int_{\partial\mathcal{K}} h \boldsymbol{u}^{\curlyvee}_{\mathrm{h}} \varphi_i \cdot \boldsymbol{n} \, ds - \int_{\mathcal{K}} h \boldsymbol{u}_{\mathrm{h}} \cdot \nabla \varphi_i \, d\boldsymbol{x} &= 0 &(30) \\ \frac{\partial}{\partial t} \int_{\mathcal{K}} h \boldsymbol{u}_{\mathrm{h}} \cdot \boldsymbol{g}^*_\alpha \varphi_i \, d\boldsymbol{x} + \int_{\partial\mathcal{K}} \boldsymbol{T}^{\curlyvee}_{\mathrm{h}} \boldsymbol{g}^*_\alpha \varphi_i \cdot \boldsymbol{n} \, ds - \int_{\mathcal{K}} \boldsymbol{T}_{\mathrm{h}} : \nabla \left(\boldsymbol{g}^*_\alpha \varphi_i \right) \, d\boldsymbol{x} &= \int_{\mathcal{K}} \boldsymbol{S}_{\mathrm{h}} \cdot \boldsymbol{g}^*_\alpha \varphi_i \, d\boldsymbol{x} + \epsilon^K_P &(31) \end{aligned}$$

where inexact quadrature is used for all integrals. Now for the lake at rest state we obtain

$$\int_{\partial\mathcal{K}} \left(P^{\curlyvee}_{\mathrm{h}} - P_{\mathrm{h}} \right) \boldsymbol{I} \boldsymbol{g}^*_\alpha \varphi_i \cdot \boldsymbol{n} \, ds + \int_{\mathcal{K}} \left(\nabla \cdot P_{\mathrm{h}} \boldsymbol{I} \right) \cdot \boldsymbol{g}^*_\alpha \varphi_i \, d\boldsymbol{x} = - \int_{\mathcal{K}} g h_{\mathrm{h}} \nabla b \cdot \boldsymbol{g}^*_\alpha \varphi_i \, d\boldsymbol{x}$$

For a proper choice of the numerical flux function verifying $P^{\curlyvee}_{\mathrm{h}} = P_{\mathrm{h}}$ in the lake at rest case, the boundary penalization term vanishes. Moreover, for any order $h_{\mathrm{h}}, b_{\mathrm{h}} \in V^p_{\mathrm{h}}$ on can show that if $h_i + b_i = \eta_0$ =const we have:

$$\nabla \cdot P_{\mathrm{h}} \boldsymbol{I} + g h_{\mathrm{h}} \nabla b_{\mathrm{h}} = \nabla \frac{\left(\sum_j \varphi_j h_j \right)^2}{2} + g h_{\mathrm{h}} \nabla b_{\mathrm{h}} \tag{32}$$

and well-balanced property is recovered. In practice, we use the quadrature order necessary for exact integration of the hydrostatic term in the plane case as in [11]. Note that the scheme is considerably different from the one of [12], as here we do not use the strong form of the equations but add a hydrostatic correction to the weak form, and moreover we use here a mixed 3d/2d-covariant form of the problem on the true sphere, while a full 3d approximation on a finite element projection of the sphere is used in the reference.

4.3. Numerical fluxes: mass conservation and well balanced

For the mixed 3d/2d formulation, all geometrical quantities are uniquely and objectively defined in 3d, so we can use practically any Riemann solver in 3d Cartesian coordinates, that is:

$$\int_{\partial\mathcal{K}} \boldsymbol{T}_{\mathrm{h}}^{\Upsilon} \cdot \boldsymbol{g}_{\alpha}^{*}\varphi_i \cdot \boldsymbol{n}\, ds = \int_{\partial\mathcal{K}} \underbrace{\boldsymbol{T}_{\mathrm{h}}^{\Upsilon} \cdot \boldsymbol{n}}_{\boldsymbol{F}_2} \cdot \boldsymbol{g}_{\alpha}^{*}\varphi_i\, ds \tag{33}$$

where $\boldsymbol{F}_2 \in \mathbb{R}^3$ is a specified numerical flux $\boldsymbol{F}_2(\mathsf{u}_L, \mathsf{u}_R)$. In practice we use Lax-Friederich flux.

We remark that the problem of using a common framework between the left and right state in the original [10] is no longer necessary since the normals are continuous at the edges. Only a change of basis is needed at this point to compute 3d velocities because they are only available from momentum update, in 2d. This is done with the right relationship in (13) and the definition of the sphere Jacobian (3). The important consequence of this is that the method proposed conserves mass exactly without any special treatment of the normals on element boundaries.

To recover also the well balanced property in presence of discontinuous data besides the addition of the hydrostatic correction in (31), as in [11] we evaluate the numerical flux at a reconstructed state u^{*} and add a high order correction term [19]. The resulting mass/momentum numerical flux reads:

$$F_1(\mathsf{u}_L, \mathsf{u}_R) \;=\; F_1(\mathsf{u}_L^{*}, \mathsf{u}_R^{*}) \tag{34}$$

$$\boldsymbol{F}_2(\mathsf{u}_L, \mathsf{u}_R) \;=\; \boldsymbol{F}_2(\mathsf{u}_L^{*}, \mathsf{u}_R^{*}) + \frac{g}{2}\left(h_L^2 - (h_L^{*})^2\right)\boldsymbol{n} \tag{35}$$

for the definition of the reconstructed state $(h^{*}, h^{*}u^{*\alpha})$ please refer to [19]. In real applications, discontinuous data b_{h}, p_{atm} arise, for example, when the correspondent fields are computed at the degrees of freedom from a local minimization problem. For the bathymetry this can be beneficial to avoid Gibbs phonomena when data is nearly discontinuous on one cell and the polynomial order is $p > 1$. For the atmospheric pressure field we assume that it is continuously interpolated at the degrees of freedom. In this case the well-balanced correction related to the inverted barometer (first line is mass correction, second line is momentum correction):

$$+\frac{1}{2}\frac{1}{g\rho_0}\begin{pmatrix} \alpha_{LF} \\ g\frac{h_R^{*}+h_L^{*}}{2}\boldsymbol{n} \end{pmatrix}(p_{atm,L} - p_{atm,R}) \tag{36}$$

is identically zero, being $p_{atm,L} = p_{atm,R}$.

Proposition. *The mixed 3d/2d-covariant DG method* (30)(31) *with numerical fluxes* (35) *is well balanced in the sense that it preserves exactly initial data verifying the balance* (16) *or* (17) *in each cell.*

Proof. similarly to [11], the proof is based on the fact that, in the lake at rest or inverted barometer case, the numerical flux in momentum equation reduces to $\boldsymbol{F}_2(\mathsf{u}_L, \mathsf{u}_R) = P_\mathrm{h}(h_L)\boldsymbol{I}\cdot\boldsymbol{n}$. Then the penalization term cancels out and right hand side is zero thanks to (32) □.

5. Computational details

5.1. Shock capturing

The applications considered in this work may involve the formation of discontinuous solutions during the computation. For tsunami simulations, wave breaking occurring in shallow areas can cause the linear DG method to develop unphysical oscillations that eventually grow in time. We cope with the possibility of non-smooth solutions with an entropy viscosity approach [20, 21] which consists in adding a diffusion-like term to the right-hand side of (6),(7). Here we discuss the details related to the implementation of the diffusive term in a spherical geometry. We consider only momentum equation since mass equation is a particular case. Given a diffusive flux tensor $\boldsymbol{G} = \mu\nabla h\boldsymbol{u}$, the DG discretization in the mixed formulation of section 3.2 writes:

$$\mathcal{I}_\mu := \int_{\mathcal{K}} \nabla\cdot\boldsymbol{G}_\mathrm{h}\cdot\boldsymbol{g}^*_\alpha\varphi_i\,d\boldsymbol{x} = \int_{\partial\mathcal{K}} \boldsymbol{G}_\mathrm{h}\cdot\boldsymbol{n}\cdot\varphi_i\boldsymbol{g}^*_\alpha\,ds - \int_{\mathcal{K}} \boldsymbol{G}_\mathrm{h} : \nabla\left(\boldsymbol{g}^*_\alpha\varphi_i\right)\,d\boldsymbol{x} \tag{37}$$

To stabilize the shocks only the volume integral is retained in practice and moreover we neglect the variation of the tangent basis so that integral (37) simplifies to:

$$\mathcal{I}_\mu = -\int_{\mathcal{K}} G^{kj}_\mathrm{h} g^{*j}_\alpha \frac{\partial\varphi_i}{\partial x^k} d\boldsymbol{x} \tag{38}$$

Note that $G^{kj}g^{*j}_\alpha = G^{\alpha k}$ is a diffusive flux tensor projected on the tangent plane. As for the advective flux, since we evolve momentum in the tangent basis, we do not have access directly to G^{kj} in Cartesian basis. However diffusive tensor components are easily recovered from relationships (13) and (24):

$$G^{kj} = \mu\frac{\partial hu^j}{\partial x^k} = \mu\frac{\partial}{\partial x^k}\left(J^{*,j\beta}_G hu^{*\beta}\right) = \mu\, hu^{*\beta}\frac{\partial g^{*j}_\beta}{\partial x^k} + \mu\, J^{*,j\beta}_G\frac{\partial hu^{*\beta}}{\partial x^k}$$

Near discontinuities the viscosity coefficient μ should be of order h_K in order to kill oscillations while in smooth regions it is expected to be below the approximation order. To this end, we follow the principles originally proposed e.g. in [20, 21] and define this coefficient starting from the total energy residual. We refer to the last references for the formulation, and to [22] and references therein for its parametrization.

5.2. Time stepping

High order temporal accuracy is achieved, as it is standard, with a SSPRK method [23]. The time step is computed according to:

$$\Delta t = CFL \, \frac{\min_{\mathcal{K}} \rho_{\mathcal{K}}}{2 \max_{f \in \mathcal{T}_{\mathrm{h}}} \alpha_{LF_f}}$$

with $\rho_{\mathcal{K}}$ the elemental inscribed circle radius and α_{LF_f} the Lax-Friederich parameter at face f. For linear stability reason one should use $CFL = \frac{1}{2p+1}$ (being k the polynomial order of the approximation), but for practical use in this work we always set $CFL = 0.5$.

6. Results

In all computations presented hereafter we have set, unless otherwise stated, $R = 6371.22 \times 10^3 \, m$, $g = 9.80616 \, m^2 s^{-1}$, $\Omega = 7.295 \times 10^{-5} \, s^{-1}$ and $\rho_0 = 1025 \, kg/m^3$. Simulations have been carried out with linear (P^1), quadratic (P^2) and cubic polynomials (P^3).

6.1. Global atmospheric tests

In this paragraph we test the DG scheme on some classical benchmarks taken from the test suite of Williamson et al. (W92) [24] and [25].

Global Steady-State Nonlinear Zonal Geostrophic Flow. *W92 Case #2* is an exact steady geostrophic equilibrium allowing to measure the order of accuracy in presence of Earth rotation. The velocity and height fields are initially given by:

$$\begin{aligned} h(\boldsymbol{x}, 0) &= h_0 - \frac{1}{g} \left(\Omega R \, u_0 + \frac{u_0^2}{2} \right) (-\cos\lambda \cos\varphi \sin\alpha + \sin\lambda \cos\alpha)^2 \\ u^{*1}(\boldsymbol{x}, 0) &= u_0 \, (\cos\lambda \cos\alpha + \cos\varphi \sin\lambda \sin\alpha) \\ u^{*2}(\boldsymbol{x}, 0) &= -u_0 \sin\varphi \sin\alpha \end{aligned} \tag{39}$$

with $gh_0 = 2.94 \times 10^4 \, m^2 s^{-2}$ and $u_0 = \frac{2\pi R}{12 days}$ and $\alpha = 0$. Grid convergence studies gave been conducted on 5 icosahedral grids, from level 1 ($\mathrm{h}_K = 3571 \, km$) to level 5 ($\mathrm{h}_K = 223 \, km$). Relative errors are evaluated following [24]:

$$e_p = \frac{||e||_{L^p}}{||h_{ex}||_{L^p}} \tag{40}$$

with $e = h - h_{ex}$ and h_{ex} the exact solution. The errors obtained at day 5 are reported on table 1 below. Convergence curves are compared in figure 1 against the results of the original [10]. To make the comparison effective, only for this experiment, we we have tried to stick to their same scheme, DG

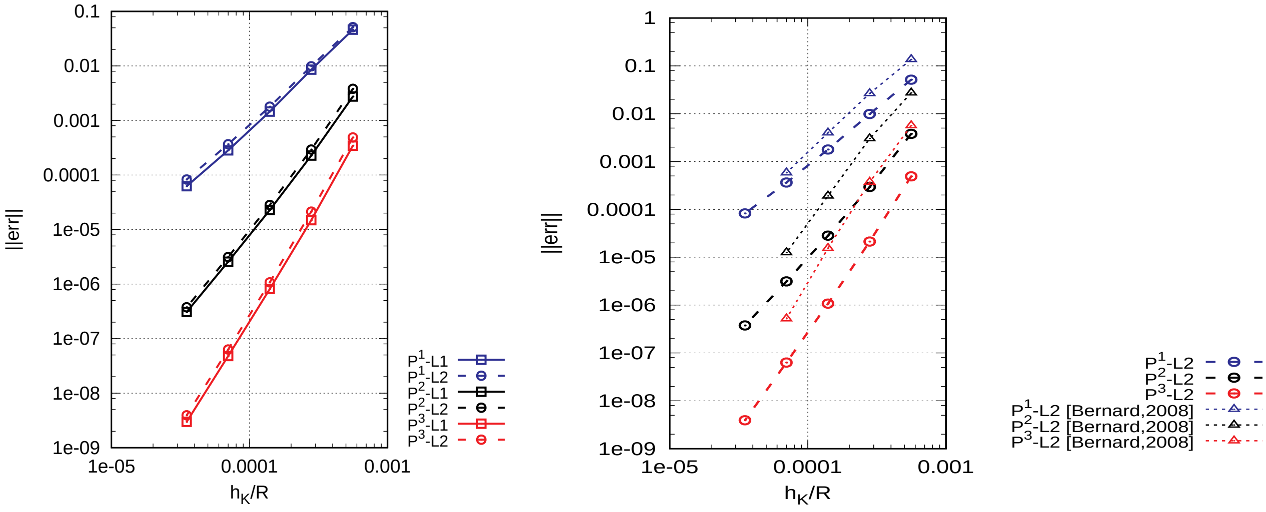

Figure 1: Global Steady-State Nonlinear Zonal Geostrophic Flow. Left: mesh convergence for L1 and L2 error norm. Right: mesh convergence for L2 error and comparison with [10].

in the weak-form (21) with Lax-Friederich flux. We have remarked that the use of the well-balanced momentum form (31) has almost no impact on the errors. At every order, theoretical order of convergence has been obtained, with smaller errors with respect to the reference. We explain this improvement by the cancellation of the geometrical error in the sphere representation. As it is customary we report on figure 2 the error maps after 5 days of simulation on the fourth grid ($\mathrm{h}_K = 446\,km$).

grid # ($\alpha = 0$)	$e_1 - P^1$	$e_2 - P^1$	$e_1 - P^2$	$e_2 - P^2$	$e_1 - P^3$	$e_2 - P^3$
1	4.6261e-02	5.1549e-02	2.7469e-03	3.8020e-03	3.4459e-04	4.8972e-04
2	8.5532e-03	9.8352e-03	2.2773e-04	2.9368e-04	1.4836e-05	2.1296e-05
3	1.4574e-03	1.7889e-03	2.2788e-05	2.8277e-05	8.1059e-07	1.0731e-06
4	2.8337e-04	3.6591e-04	2.5750e-06	3.1282e-06	4.7899e-08	6.3057e-08
5	6.2480e-05	8.2598e-05	3.0803e-07	3.7606e-07	2.9741e-09	3.9206e-09
Order	2.3980	2.3319	3.2711	3.3160	4.1919	4.2260

Table 1: Global Steady-State Nonlinear Zonal Geostrophic Flow. L^1,L^2 error norm and convergence rate.

Zonal Flow over an Isolated Mountain. *W92 Case #5* is a perturbation of the previous test. The initial velocity and height fields are equal to (39) with $\alpha = 0$, $h_0 = 5960\,m$ and $u_0 = 20\,m/s$. An isolated

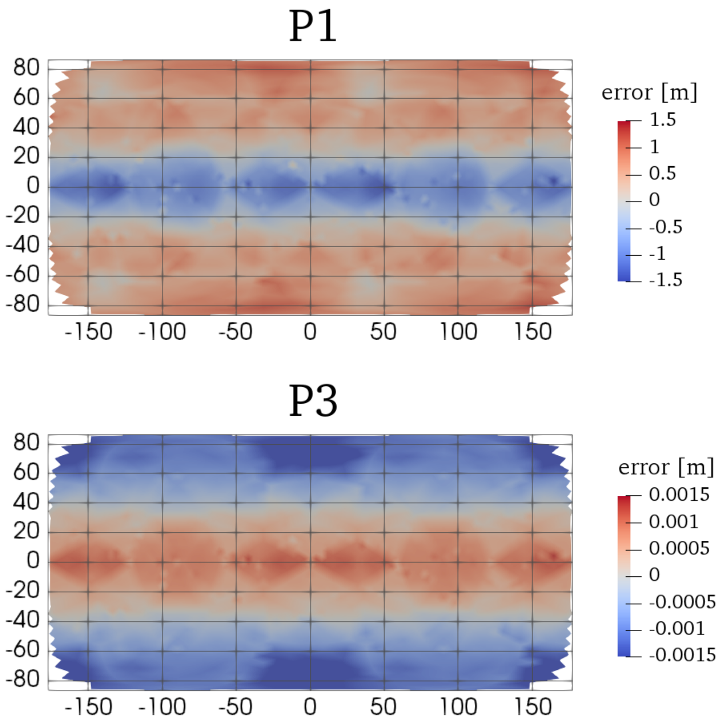

Figure 2: Global Steady-State Nonlinear Zonal Geostrophic Flow. Error plot. Top: P^1. Bottom: P^3. Note that color scale change of one order of magnitude for each plot.

mountain is added:

$$b = b_0 \left(1 - \frac{r}{R}\right) \tag{41}$$

with $b_0 = 2000\,m$, $R = \pi/9$, $r^2 = \min(R^2, (\varphi - \varphi_0)^2 + (\lambda - \lambda_0)^2)$ and with the center of the cone in $(\varphi_0, \lambda_0) = (3/2\pi, \pi/6)$. Simulations are performed on the fourth icosahedral grid ($\mathrm{h}_K = 446\,km$). Figure 3 provides height contour lines for P^1,P^2 and P^3 computations after 15 days of physical time. For this case one typically checks the conservation of total mass and energy

$$E = h\left(\frac{1}{2}||\boldsymbol{u}||^2 + g\frac{h}{2} + gb\right) \tag{42}$$

Mass error should be only related to round-off errors. Regarding the energy, the proposed scheme have no provable energy conservation properties, which makes the definition of the actual discrete evaluation of the energy somewhat arbitrary. In practice, here the energy is computed directly from nodal quantities, and then integrated using the high order finite element approximation. After 15 days mass is conserved within a relative error of $1e - 13$. Relative energy conservation error is reported on the right column in figure 3: it is comparable to or better than those typically reported in literature. In the same figure we compare with a second order residual distribution scheme proposed by the authors [16], with a third order FV scheme on a cubed sphere [5] and with the high resolution results by the German Weather Service (DWD) `http://icon.enes.org/swm/stswm/node5.html`.

Unstable Jet. The last global test taken from [25] consists of a geostrophically balanced mid-latitude jet, to which a small perturbation is added to initiate the instability. We use this test to confirm that the polar treatment has no impact on the numerical solution and on its derivatives. We look to the vorticity field for P^1, P^2 and P^3 solutions but with two different z_{lim}, the one used in other experiments $z_{lim} = 0.9R$ and $z_{lim} = 0.75R$ for which the polar cap interface falls exactly into the jet. Mesh convergence has been carried on two successive icosahedral grids (level 5 and 6, respectively $223\,km$ and $111\,km$), see figures 4, 5. At both mesh level, P^1 solution is insufficient to support the vortex evolutions. Increasing the order, P^2, P^3 computations at mesh level 5 provide the correct dynamics but the vorticity contours are a little bit jagged. At level 6 much of the jaggedness disappears.

6.2. Small amplitude barotropic waves

With this test we look to the impact of the well balancing correction for classical oceanic applications such as tidal and surge waves. We have taken a basin spanning from 0° to $25°E$ and from $35°N$ to $55°N$. The bathymetry is a smooth Gaussian hump mimicking a continental shelf and an isolated mountain:

$$b = \max\left(b_0 \exp\{-r_0^2/R\}, b_1\,(1 - r_1/R)\right)$$

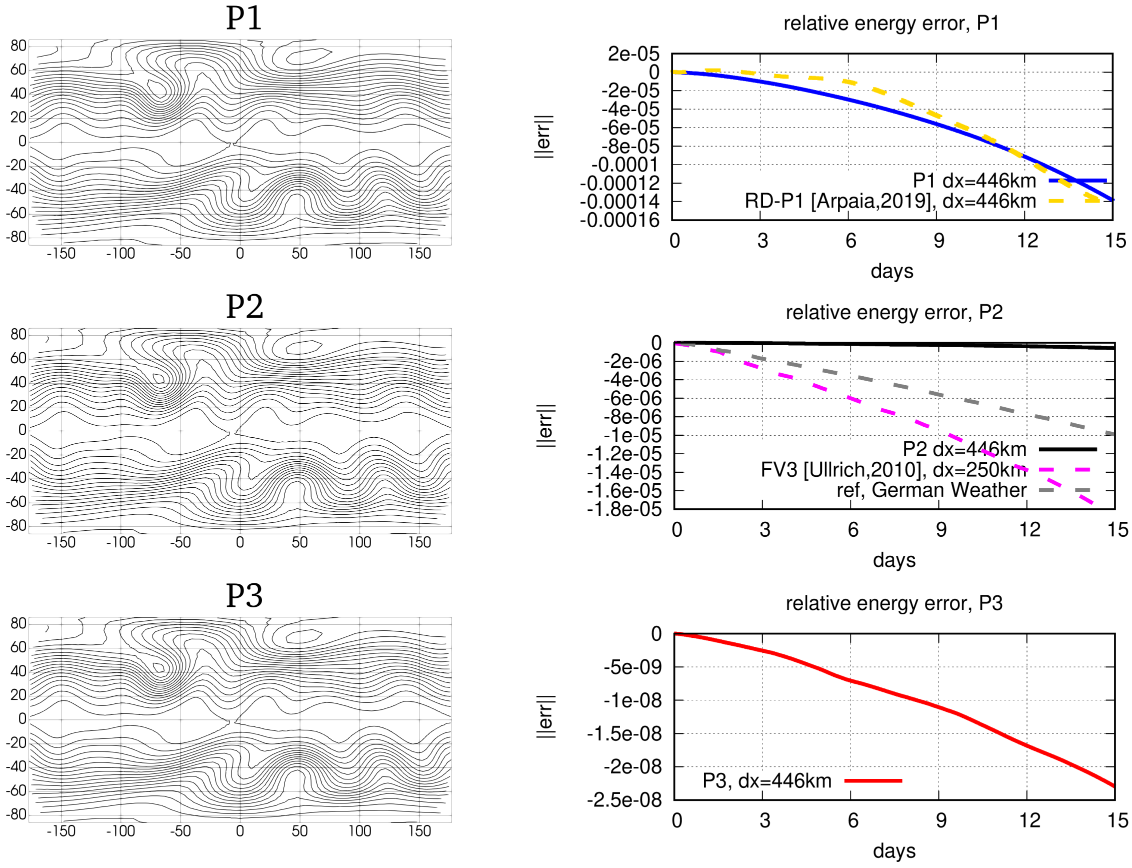

Figure 3: Zonal flow over an isolated mountain. Left: Snapshot at day 15 (depth contour levels from 5050 m to 5950 m-intervals of 50 m). Right: relative energy error (results from [5, 16] and from the DWD reported for comparison where relevant)

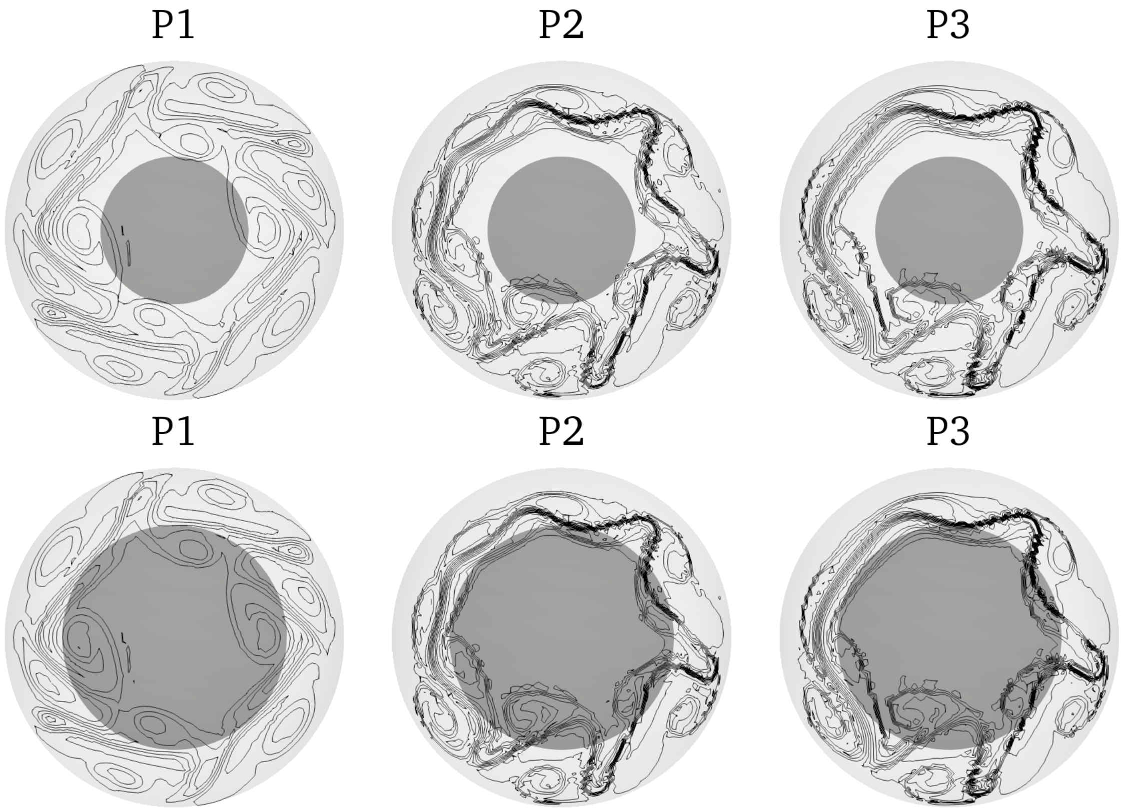

Figure 4: Unstable Jet. Coarse resolution $h_K = 223\,km$. Dark grey area represents a circle with radius $R\sqrt{1-\left(\frac{z_{lim}}{R}\right)^2}$ (polar cap region). Contour levels from $-1.1e-4$ to $1.5e+4$.

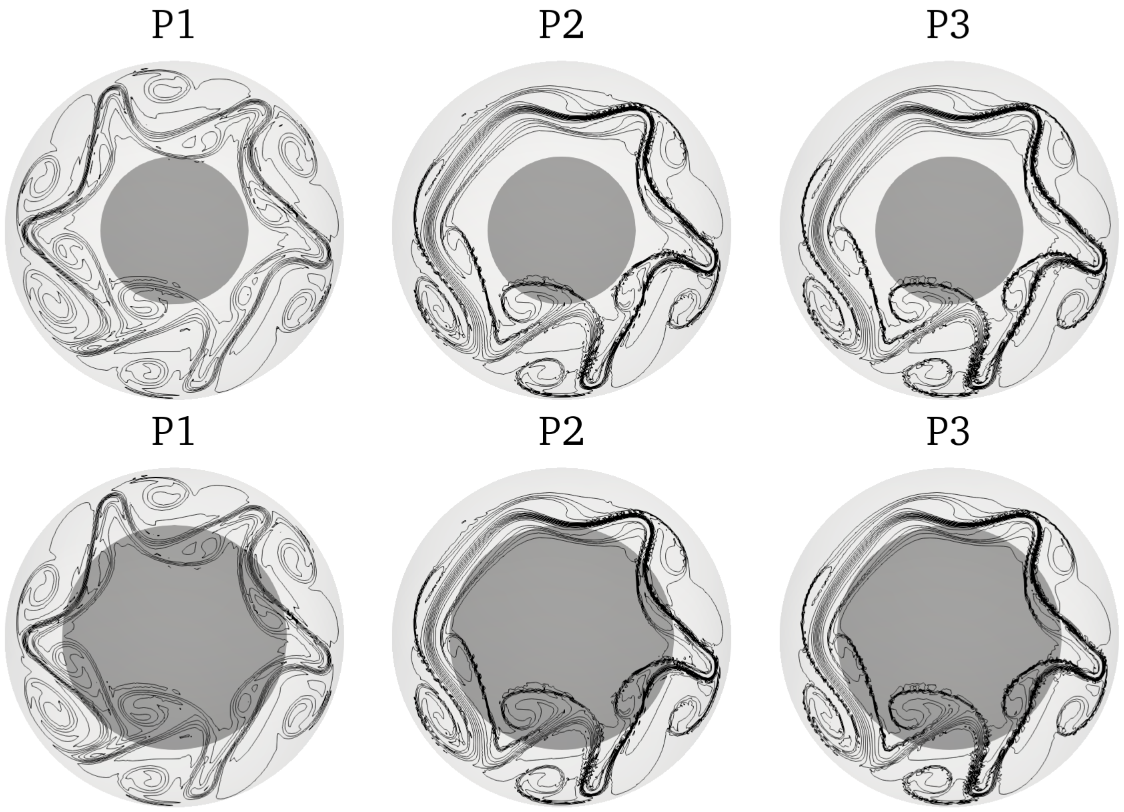

Figure 5: Unstable Jet. Fine resolution $h_K = 111\,km$. Dark grey area represents a circle with radius $R\sqrt{1-\left(\frac{z_{lim}}{R}\right)^2}$ (polar cap region). Contour levels from $-1.1e-4$ to $1.5e+4$.

with $b_0 = 2000\,m$, $R_0 = \pi/12$, $r_0^2 = 8.5(\varphi - \varphi_0)^2 + (\lambda - \lambda_0)^2$, $(\varphi_0, \lambda_0) = (0, \pi/4)$ and $b_1 = 4000\,m$, $R_1 = 5\pi/180$, $r_1^2 = (\varphi - \varphi_1)^2 + (\lambda - \lambda_1)^2$, $(\varphi_1, \lambda_1) = (10\pi/180, 48\pi/180)$. The mesh is an unstructured triangulation with topology shown in the top of figure (6) and constant mesh size $\mathrm{h}_K = 100\,km$. For a lake at rest state with initial level $\eta_0 = 5000\,m$ the well balanced spherical formulation (31) exhibits a maximum perturbation of the velocity norm in the range $1e-12$ to $1e-13$ depending on the polynomial order. After this well-balancing test, a small amplitude tidal signal $\eta_0 + A\sin(\frac{2\pi}{T}t)$ is imposed at the north boundary ($A = 0.01\,m$, $T = 12.42\,hrs$). The eastern boundary is a wall to let a southward propagating barotropic Kelvin wave develop. We compare (31) against the non-well balanced scheme based on the weak formulation (21). In the left block of figure (6) two snapshots of upwelling/downwelling at the lateral wall show that the P1 solution of the non well-balanced scheme is affected by small wiggles. The perturbation tend to disappear, as expected, with mesh resolution (see right block) and with polynomial order (not shown). A second test has been carried by forcing a surge wave with a small amplitude atmospheric depression:

$$p_{atm}(\boldsymbol{x}, t) = p_0 - \Delta p \exp\left(\frac{r(\boldsymbol{x}, t)}{\sigma^2}\right)$$

with r the distance from the center of the storm which is translating southward at constant speed U. The parameters are set to $p_0 = 101\,kPa$, $\Delta p = 0.3\,kPa$, $\sigma = 350\,km$ and $U = \sqrt{100g}$. In figure (7) we show the impact of the well-balanced correction. Again, at the coarse resolution (left block), the small-amplitude gravity waves that propagates faster then the storm are much wiggled in the non well-balanced case. Increasing mesh resolution (see right block) and polynomial order (not shown) makes again such wiggles negligible.

6.3. Circular hump centered at the equator

This is a test proposed in [6]. The initial condition is a circular depth disturbance at the equator:

$$h(\boldsymbol{x}, 0) = \begin{cases} 2 & \text{if } \arccos(\cos(x^1)\cos(x^2)) \le 0.2 \\ 0.2 & \text{otherwise} \end{cases}, \qquad \boldsymbol{u}(\boldsymbol{x}, 0) = 0 \tag{43}$$

This initial condition is symmetric about the point $(x^1, x^2) = (0°, 0°)$, and should remain symmetric in absence of rotation. Shock capturing is necessary to well represent the discontinuity. We run computations on two half sphere meshes generated with `gmsh`: a coarse one with 2436 points; a fine one with 9187 points. In figure 8 we compare the solution contours obtained with P1/P2 on the coarse mesh against a P1 solution on the fine mesh. We observe mesh/order convergence for this non-smooth case. At $t = 0.9$ the P2 solution on the coarse mesh is of the same order of accuracy of the P1 solution on the fine mesh.

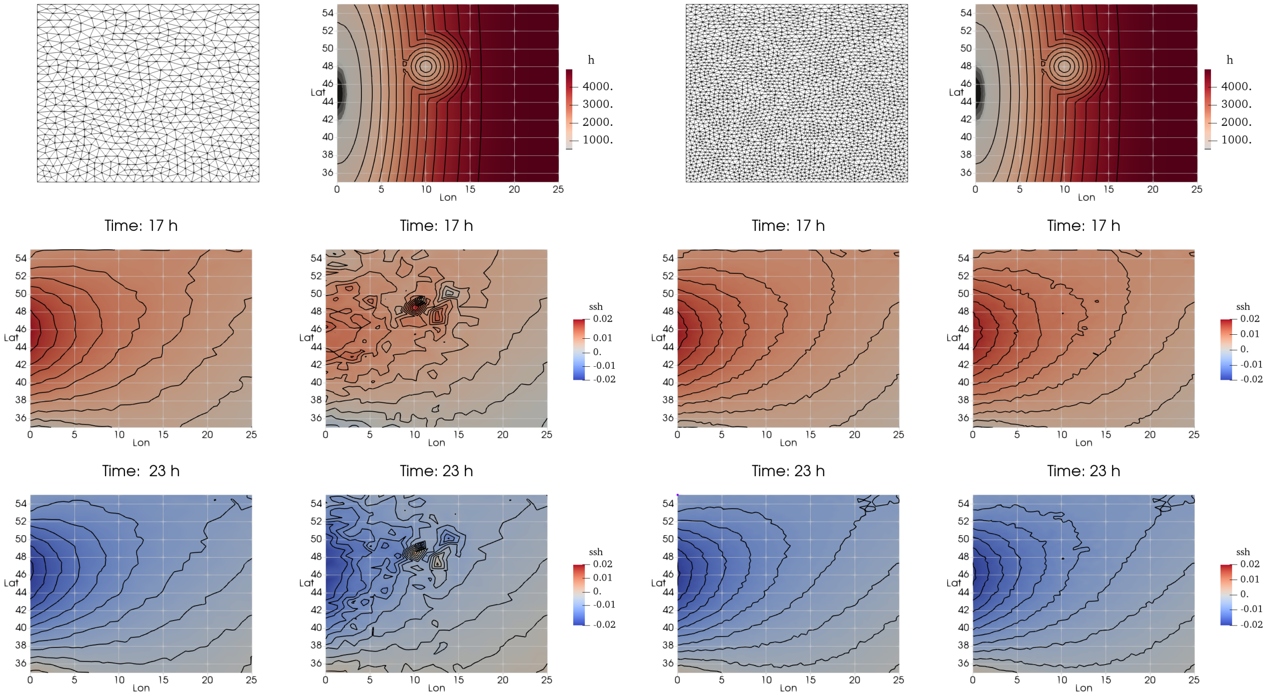

Figure 6: Small amplitude tidal wave. Coarse $h_K = 100\,km$ (left block) and fine $h_K = 50\,km$ (right block) simulation. Top: mesh and bathymetry. Middle and bottom: snapshot of the free surface at $t = 18h$ and $23h$. Left: well balanced scheme. Right: non-well balanced scheme. Contour levels are from $-0.02\,m$ to $0.02\,m$ in intervals of $0.002\,m$.

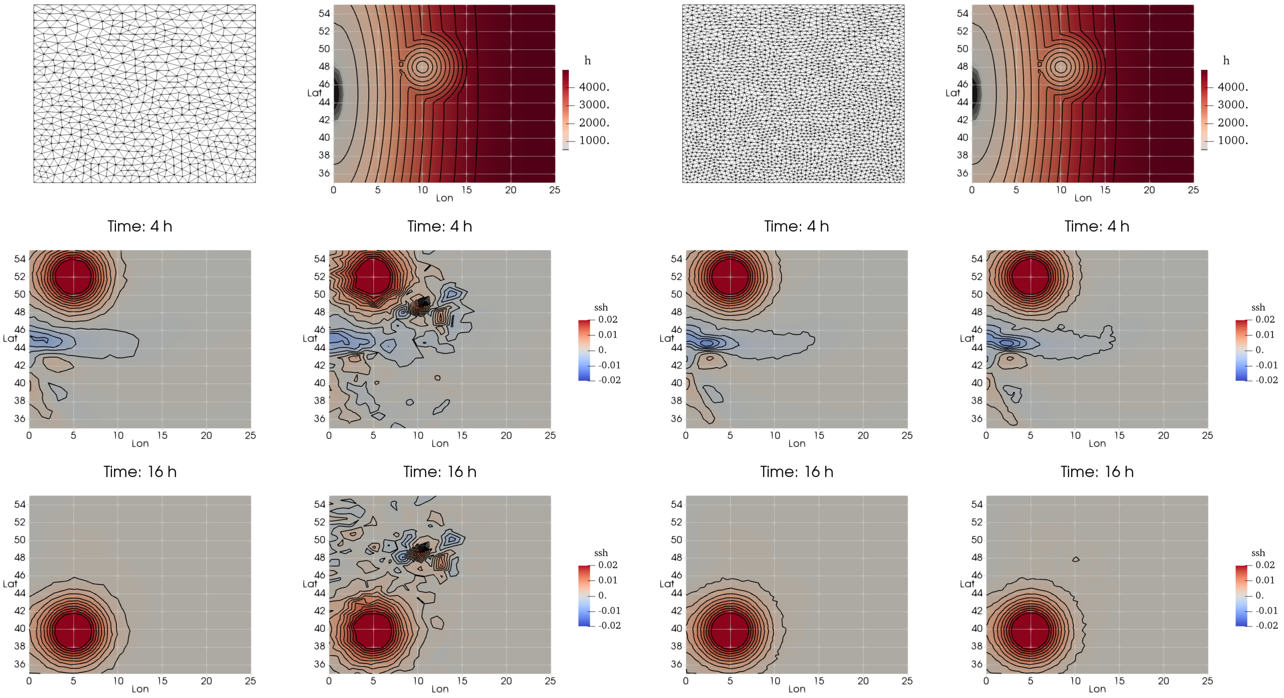

Figure 7: Small amplitude surge wave. Coarse $h_K = 100\,km$ (left block) and fine $h_K = 50\,km$ (right block) simulation. Top: mesh and bathymetry. Middle and bottom: snapshot of the free surface at $t = 4h$ and $16h$. Left: well balanced scheme. Right: non-well balanced scheme. Contour levels are from $-0.02\,m$ to $0.02\,m$ in intervals of $0.002\,m$.

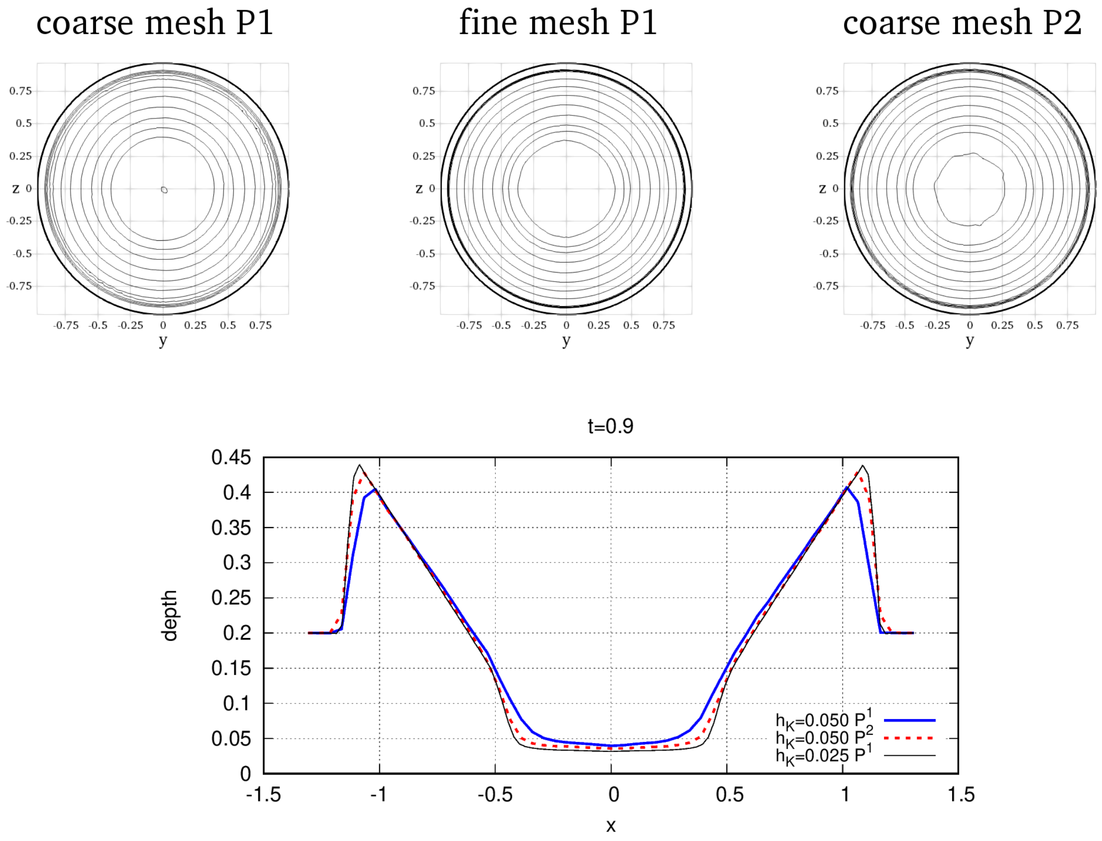

Figure 8: Circular Hump. Contour levels at $t = 0.9$ from $0.04\,m$ to $0.5\,m$ in intervals of $0.045\,m$. Bottom: cut along the the equator

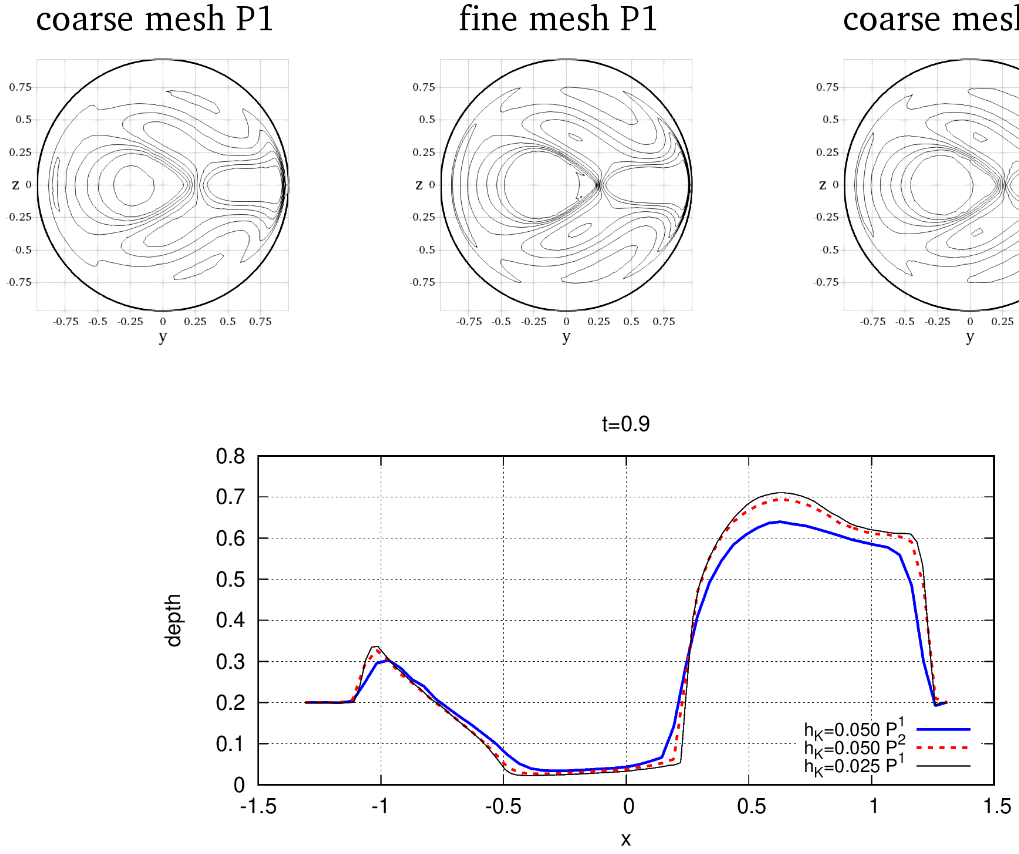

Figure 9: Circular Hump with rotation. Contour levels at $t = 1.2$ from $0.04\,m$ to $0.5\,m$ in intervals of $0.045\,m$. Bottom: cut along the the equator

We repeat the same test adding rotation effects. We set the dimensionless rotation rate to $\Omega = 5$. In figure 9 we report depth contour lines at $t = 1.2$. As in the previous case, we observe the higher resolution obtained with P2 scheme both in smooth and discontinuous regions.

6.4. Realistic external gravity waves simulations

Finally, to show the potential of this method, we perform two realistic simulations in the Caribbean Sea. The computational domain, the bathymetry and the mesh were specified by the consortium of the project Interreg Carib-Coast (https://www.interreg-caraibes.fr/carib-coast). The domain in figure 10 spans from $50°W$ to $84.7°W$ and from $8.4°N$ to $22.1°N$. The bathymetry at the degrees of freedom is computed from GEBCO (`www.gebco.net`) and from SHOM for the French west indies (`https://data.shom.fr/donnees`). To avoid wetting/drying of cells near the coastline, we have filtered the bathymetry at land masses contained in the computational domain with $b_{filt} = \min(b, -1)$. Even if, during the computation, we have observed wetting/drying at some cells, the filter assures that all the cells are wet for the initial condition, avoiding well-balancing problems for partly dry cells, not addressed in the present study. The mesh has variable mesh size ranging from $h_{K,max}$ in deep ocean to $h_{K,min}$ at the coast in correspondence of Martinique, Guadaloupe and Saint Martin islands, which represent some interest sites of the Carib-Coast project. A fine and a coarse mesh have been generated, respectively with $h_{K,min} = 300\,m$, $h_{K,max} = 10\,km$ and $h_{K,min} = 600\,m$, $h_{K,max} = 20\,km$. A Manning friction term, with $n = 0.025$ has been added to the system.

6.4.1. Tsunami in Carribean Sea

The initial tsunami waveform is associated with a random rupture of the Lesser Antilles subduction zone. We use the fault configuration proposed by Feuillet et al. characterized by a magnitude $M_w = 8.4$ (for the fault parameters see [26]). Randomness is associated to the heterogeneity of the fault slip which is computed by a Karuhnen-Loeve expansion [27]. Then, the initial waveform is the solution of the Okada linear model. We have equipped the domain with several gauges placed in the near and far-field. In the near-field we distinguish coastal gauges in bays or harbours (Point-a-Pitre, Fort-de-France) and nearshore gauges on the continental shelf (Martinique NE, Martinique W). At far-field we have placed the gauges in the Carribean sea (Kingston) and close to east boundary (Atlantic) in order to look both to tsunami propagation after the wave has passed the Antillean Arch and free propagation in deep ocean. In figure 12 we report the sea surface height recorded at the gauge stations for P1/P2 simulations on the coarse mesh and we compare them with the P1 simulation on the fine mesh. The coarse P2 solution has roughly the same accuracy of the fine P1 solution in the near-field and it is superior for far-field propagation. For the near-field gauges the P1 solution captures sufficiently well the incoming, trapped and reflected wave train, even if the leading wave peak is slightly underestimated with respect to P2 ($40\,cm$ at Point-a-Pitre). For far-field gauges P1 solution is very diffusive, probably due to the simple Lax-Friederich flux employed in this study. Similar results emerge from the snapshot of the sea surface height at $t = 5400\,s$ 11. In figure 12, beyond mesh and order convergence we have validated the simulation against the structured high order FV code `FUNWAVE-TVD` [28] on a regular grid with $\Delta x = 800\,m$ (which has roughly the same degrees of freedom of the P2 coarse simulation). The comparison is valid for the first two hours (after FUNWAVE-TVD solution is polluted by wave reflection from the boundary, see the gauge Atlantic Ocean close the western boundary).

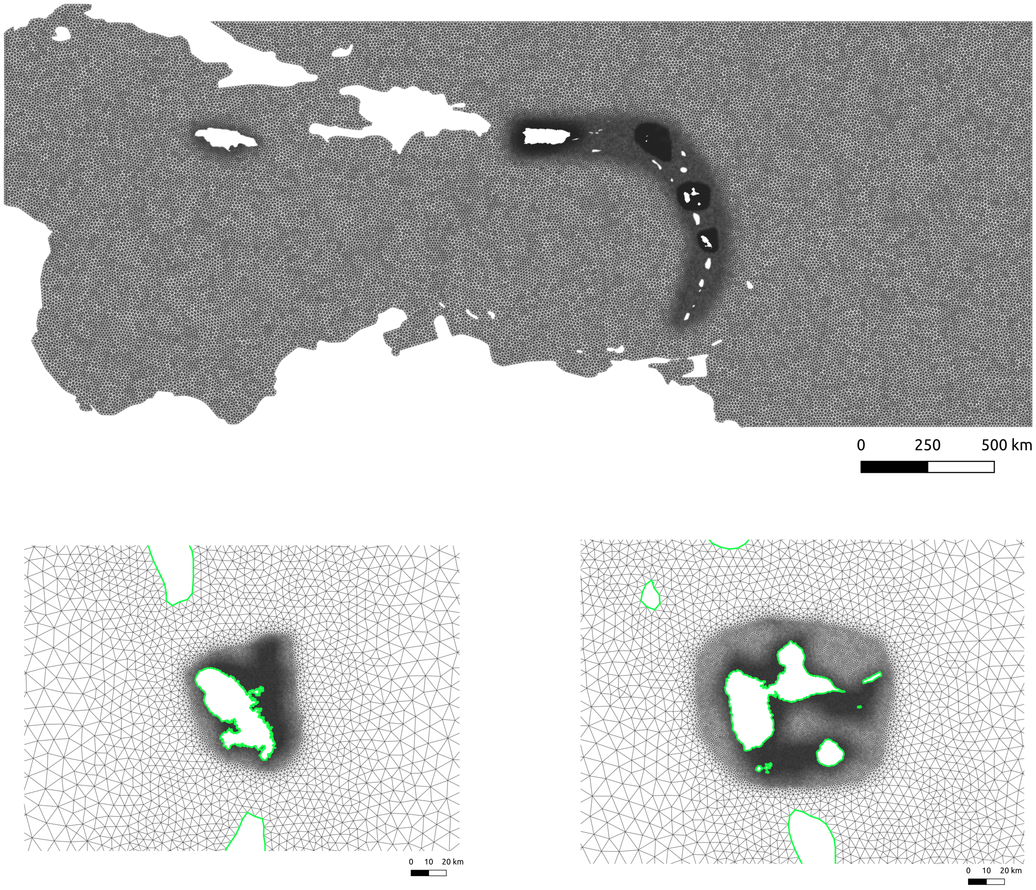

Figure 10: Realistic simulations in Caribbean Sea. Top: Full fine mesh. Bottom: Zoom of the fine mesh in correspondence of Martinique and Guadalupe island.

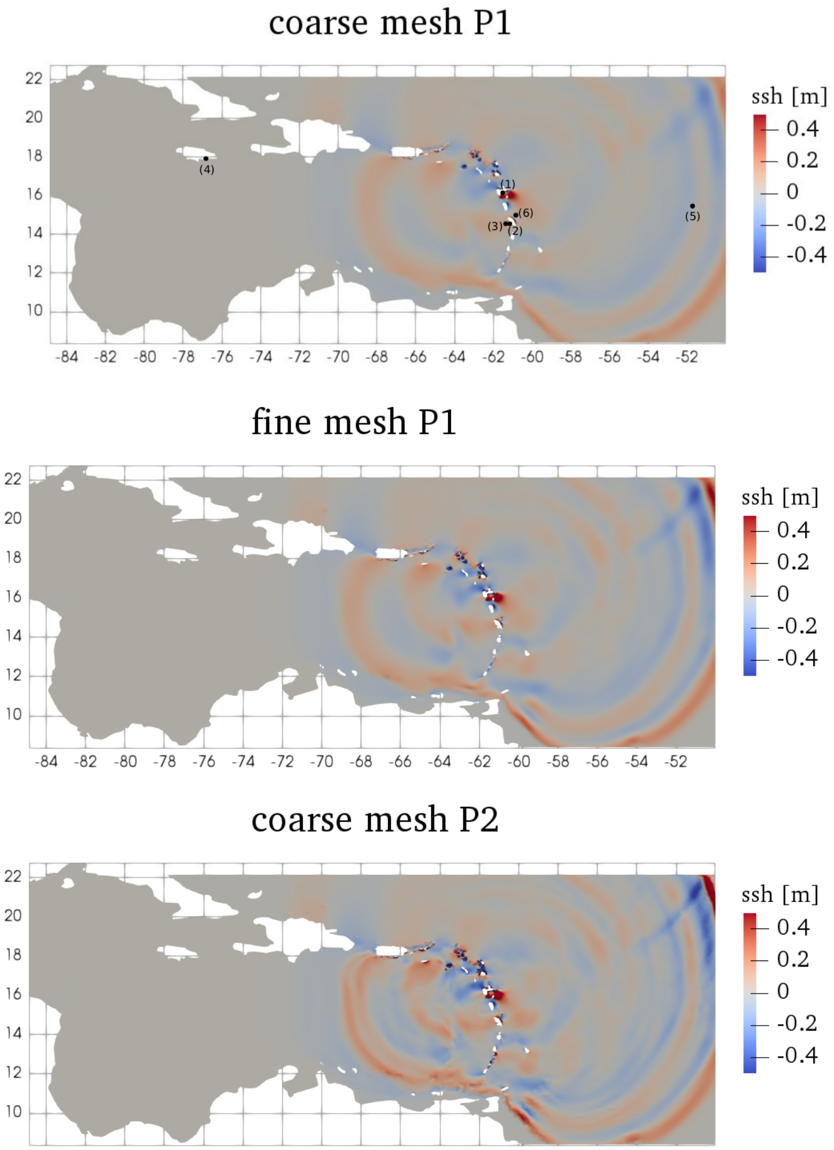

Figure 11: Tsunami in the Carribean Sea. Color map of sea surface height η after $5400\,s$. Numbers (1) to (6) in the top picture show the position of the six stations considered in Figure 12, which corresponds to: (1) Pointe-a-Pitre, (2) Fort-de-France, (3) Martinique W, (4) Kingston, (5) Atlantic Ocean, (6) Martinique NE.

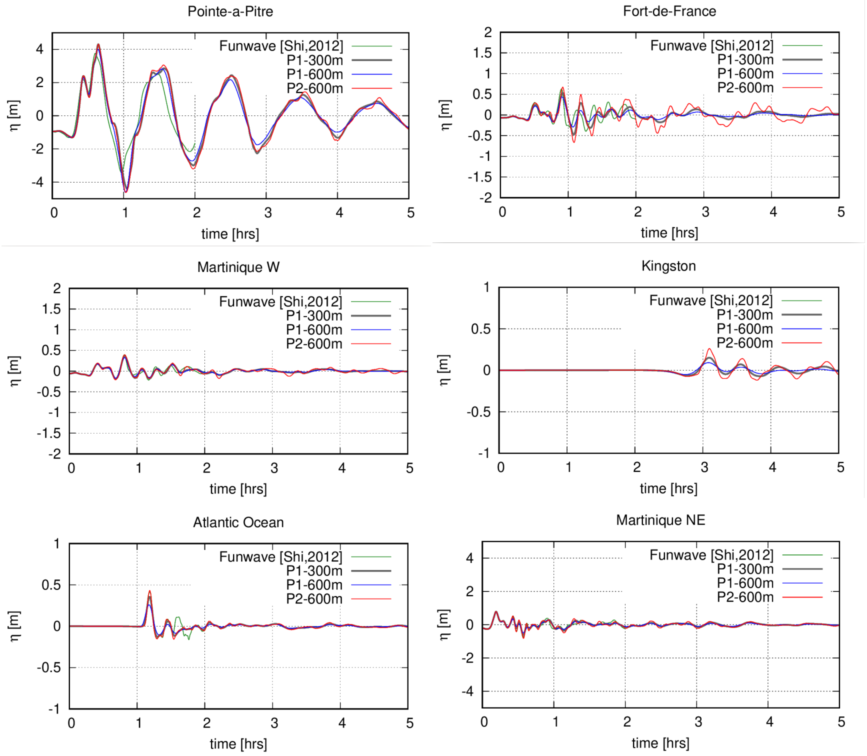

Figure 12: Tsunami in the Carribean Sea. Water height recorded at the gauge stations located at Point-a-Pitre (top-left), Fort-de-France (top-right), Martinique W (middle-left), Kingston (middle-right), Atlantic Ocean (bottom-left) and Martinique NE (bottom-right)

6.4.2. Irma hurricane

We perform the simulation of the atmospheric surge produced by the passage of hurricane Irma in the Caribbean sea (from 30th August 2017 to 14th September 2017). As known, such phenomena link up great depressions and strong winds, leading to sea level rise and flooding risk at the coast. In order to account for atmospheric forcing, the source term of the shallow water equations has to be modified as shown in (3), with the wind force f_w defined by:

$$f_\text{w} = c_D \frac{\rho_{air}}{\rho_0} |\boldsymbol{u}_{10}| \boldsymbol{u}_{10} \tag{44}$$

where ρ_{air} is the air density, $\boldsymbol{u}_{10}$ is the wind velocity field ten meters above the ground and c_D is the wind stress coefficient as proposed by Charnock [29] with Charnock parameter set to 0.022 [30]. To construct the hurricane pressure and wind fields, we used information issued from the NOAA IBTRACKS [31] database and we applied the Holland parametric model [32] Computed hurricane winds are, then, converted to surface winds and averaged over 10 minutes. After that, cyclonic wind and pressure fields are finally merged with data from CFSR model [33] in order to represent large-scale atmospheric conditions in the whole computational domain. Our simulations run from 05th September 2017 to 08th September 2017, simulating the hurricane strike on Caribbean French islands, Virgin islands and Puerto Rico. Figure 13 shows the hurricane surge propagation, simulated by the P1 coarse mesh. Indistinguishable results, at this scale, are obtained using the P2 coarse mesh, thus they are not reported here. Several NOAA/NOS and SHOM tide-gauges are available in the area, allowing to validate our simulations against real observations. Measured sea level is the result of several components: the tide, a seasonal adjustment due to baroclinicity [34], the setup due to breaking waves and, finally, the atmospheric surge due to wind and pressure. The first three components cannot be reproduced by our model. Therefore, before comparison, we processed raw signals such as to remove the tide and we applied a mean sea level offset to account for baroclinicity [35]. In this way, we were able to produce the pictures of figure 14, comparing simulations and observations at four gauges located close to the hurricane track. We can appreciate a global agreement between computed water levels by both P1 and P2 simulations and historical data. The use of P2 approximations, in this case, leads to very few improvements in the results, only noticeable on the pick representation at the location closest to the hurricane track: Saint Martin and Lameshur. Discrepancies in the results may be due to different factors, such as the parametric reconstruction of hurricane pressure and wind fields. Figure 15 compares air pressure forcing to available observed data at Charlotte Amalie and Culebra stations. Clearly, the depression pick is quite well reproduced at Charlotte Amalie, closer to the cyclone track, while it is greatly underestimated at Culebra, the farest station. This is probably the primary cause of the surge underestimation sketched in Figure 14. Other source of discrepancies may be due to wave setup contribution to observed water level, and/or the coarse representation of the insular shelf ($> 1km$) in the computational mesh of the Carib-Coast project. Further investigations could improved the results, but this is beyond the purposes of this work and they are not performed here.

7. Conclusion

In this work we have discussed an efficient and accurate formulation of the spherical Shallow Water equations in the form originally proposed in [10] which implies a mixed 3d/2d treatment: the time derivative is expressed in 2d form while the right hand side is formulated in 3d Cartesian form. We have shown that using, for the 2d part, covariant vector basis, the implementation simplifies and the accuracy increases. In this work we have opted for a Discontinuous Galerkin discretization but the mixed 3d/2d-covariant form is in principle also more amenable to a continuous Finite Elements discretization w.r.t to the original [10]. In particular local mass matrix goes back to the standard block-diagonal form, line integrals or Riemann Problem do not imply tensor/vector rotation thanks to the continuity of the normals at the edges. We have also discussed a Well-Balanced form of the resulting DG scheme resorting the hydrostatic pressure term to the strong form. Finally with a realistic tsunami and an historical storm surge simulation we have validated the method for two different oceanographic applications.

Ongoing work is devoted to extension of the discretization of the 3d/2d-covariant Shallow Water equations to stabilized continuous Finite Element (SUPG or Continuous Interior Penalty see e.g. [36] and references therein), and to one to one comparison with the current implementation.

Acknowledgments

Work partially funded by the Carib-Coast INTERREG project (https://www.interreg-caraibes.fr/caribcoast). Some of the computations presented in this paper were carried out using the BRGM experimental testbed. All the developments presented have been implemented in the platform `Aerosol/Uhaina` developed by INRIA,IMB and EPOC. In particular we are very grateful to Vincent Perrier for the time dedicated to us on the Aerosol library and for its availability all along the implementation of the present work.

References

[1] D. Williamson, The evolution of dynamical cores for global atmospheric models, J. Meteorol. Soc. Jpn. 85 (2007) 241–269.

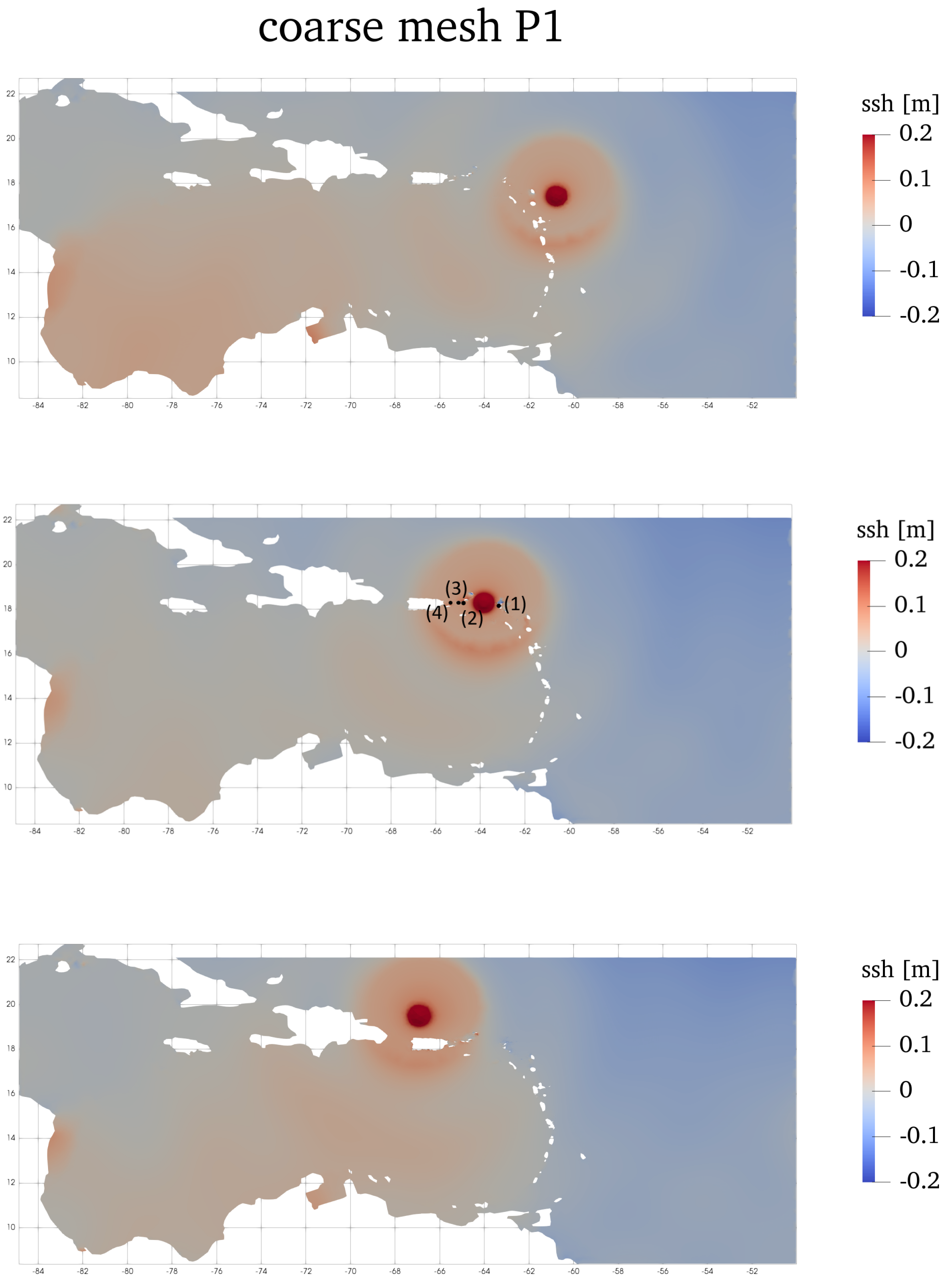

coarse mesh P1

Figure 13: Hurricane Irma. Color map of simulated surge at $02am$ on 06^{th} September 2017 (top), at $2pm$ on 06^{th} September 2017 (middle) and at $2am$ on 07^{th} September 2017 (bottom). Numbers (1) to (4) in the middle picture show the position of the four stations considered in Figure 14, which respectively correspons to: (1) Saint Martin, (2) Lameshur Bay, (3) Charlotte Amalie, (4) Culebra.

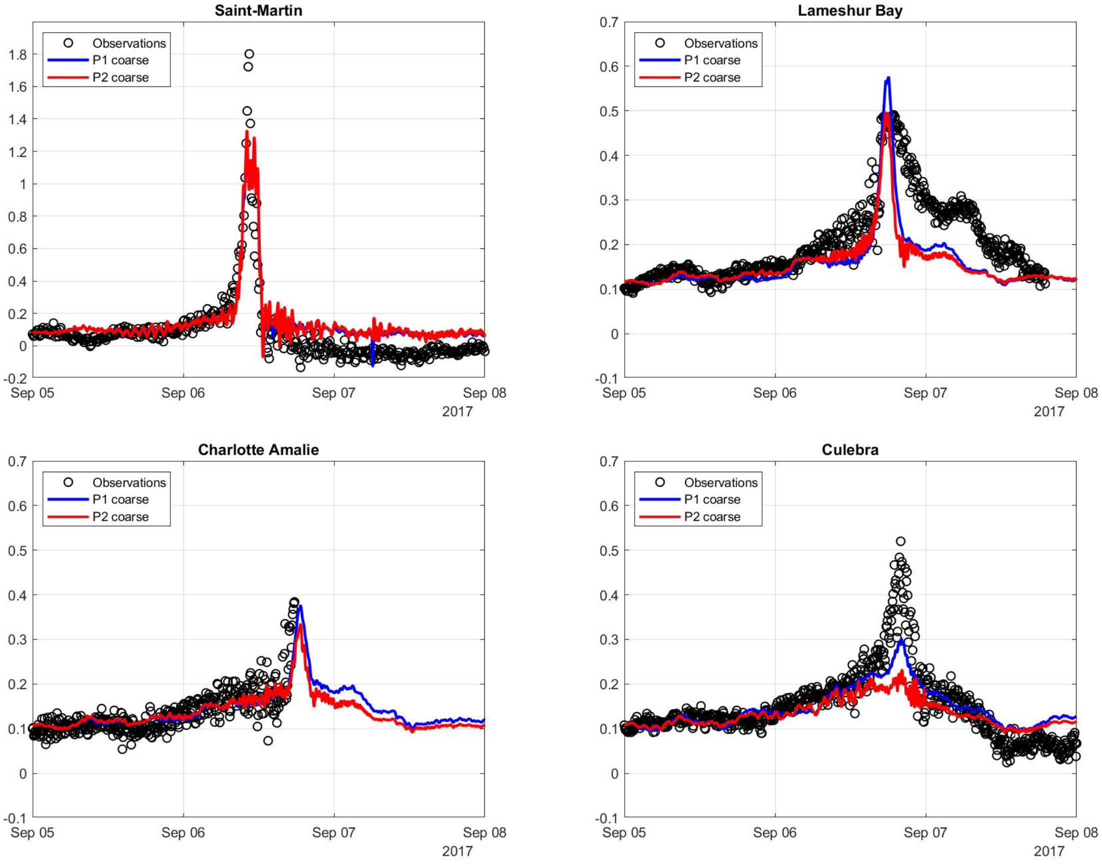

Figure 14: Hurricane Irma. Comparison of simulated sea surface height signals (scale in meters) at a selection of gauge stations, located at Saint Martin (top-left), Lamashur Bay (top-right), Charlotte Amalie (bottom-left) and Culebra (bottom-right).

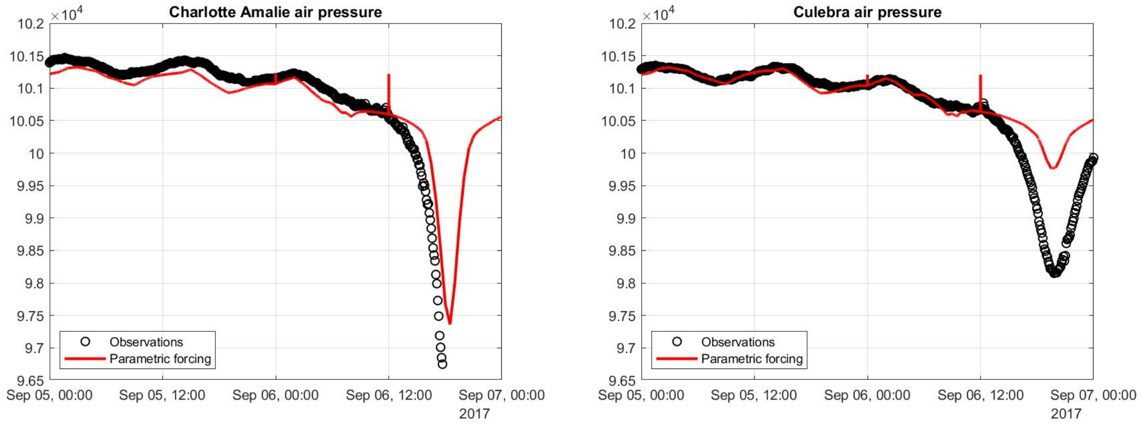

Figure 15: Hurricane Irma. Computed air pressure field is compared against observations (scale in Pa) at Charlotte Amalie (left) and Culebra (right) stations.

[2] A. Kageyama, T. Sato, "Yin-Yang grid": An overset grid in spherical geometry, Geochem. Geophys. Geosyst. 5 (2004) Q09005.

[3] C. Ronchi, R. Iacono, P. S. Paolucci, The "cubed sphere": A new method for the solution of partial differential equations in spherical geometry, J. Comput. Phys. 124 (1996) 93–114.

[4] R. D. Nair, S. J. Thomas, R. D. Loft, A discontinuous galerkin transport scheme on the cubed sphere, Monthly Weather Review 133 (2004) 814–828.

[5] P. A. Ullrich, C. Jablonowksi, B. Van-Leer, High-order finite-volume methods for the shallow water equations on the sphere, J. Comput. Phys. 229 (2010) 6104–6134.

[6] J. A. Rossmanith, A wave propagation method for hyperbolic systems on the sphere, J. Comput. Phys. 213 (2006) 629–658.

[7] G. Madec, M. Imbard, A global ocean mesh to overcome the north pole singularity, Climate Dynamics 12 (1996) 381–388.

[8] J. Coté, A Lagrange multiplier approach for the metric terms of semi-Lagrangian models on the sphere., Quart. J. R. Met. Soc. 114 (1988) 1347–1352.

[9] F. X. Giraldo, J. S. Hesthaven, T. Wartburton, Nodal high-order discontinuous galerkin methods for the spherical shallow water equations, J. Comput. Phys. 181 (2002) 499–525.

[10] P. E. Bernard, J. F. Remacle, R. Comblen, V. Legat, K. Hillewaert, High-order discontinous Galerkin schemes on general 2D manifolds applied to the shallow water eqautions, J. Comput. Phys. 228 (2009) 6514–6535.

[11] Y. Xing, X. Zhang, Positivity-preserving well-balanced discontinuous galerkin methods for the shallow water equations on unstructured triangular meshes, Journal of Scientific Computing 57 (2013) 19–41.

[12] F. X. G. B. Bonev, J. S. Hesthaven, M. A. Kopera, Discontinuous galerkin scheme for the shallow water equations with application to tsunami modeling and prediction, J. Comput. Phys. 362 (2018) 425–448.

[13] A. Bermudez, M. E. Vazquez-Cendon, Upwind methods for hyperbolic conservation laws with source terms, Comput. Fluids 235 (8) (1994) 1049–1071.

[14] A. E. Gill, Atmosphere-Ocean Dynamics, Academic, San Diego, Calif., 1982.

[15] D. Mercer, J. Sheng, R. J. Greatbatch, J. Bobanovic, Barotropic waves generated by storms moving rapidly over shallow water, J. Geophys. Res. 107(C10) (2002) 3152.

[16] L. Arpaia, M. Ricchiuto, Well-balanced residual distibution for the ALE spherical shallow water equations on moving adaptive meshes, J. Comput. Phys. (405).

[17] F. Bouchut, J. LeSommer, V. Zeitlin, Frontal geostrophic adjustment and nonlinear-wave phenomena in one dimensional rotating shallow water, J. Fluid Mech. Part 2: high-resolution numerical simulations 514 (2004) 35–63.

[18] D. Kopriva, Metric identities and the discontinuous spectral element method on curvilinear meshes, Journal of Scientific Computing 26 (2006) 301–327.

[19] E. Audusse, F. Bouchut, R. K. M.-O. Bristeau, B. Perthame, A fast and stable well-balanced scheme with hydrostatic reconstruction for shallow water flows, SIAM Journal of Scientific Computing 25 (2004) 2050–2065.

[20] J. L. Guermond, R. Pasquetti, B. Popov, Entropy viscosity method for nonlinear conservation laws, J. Comput. Phys. 230 (2011) 4248–4267.

[21] R. Pasquetti, Viscous stabilizations for high order approximations of saint-venant and boussinesq flows, In Global Tsunami Science: Past and Future, Springer International Publish- ing., 2017, pp. 3671–3692.

[22] A. G. Filippini, S. D. Brye, V. Perrier, F. Marche, M. Ricchiuto, D. Lannes, P. Bonneton, UHAINA: A parallel high performance unstructured near-shore wave model, XVmes Journées Nationales Geénie Cotier - Génie Civil. 2018.

[23] S. Gottlieb, C. W. Shu, E. Tadmor, Strong stability-preserving high-order time discretization methods, SIAM Rev. 43 (2001) 89–112.

[24] D. L. Williamson, J. B. Drake, J. J. Hack, R. Jakob, P. N. Swarztrauber, A standard test set for numerical approximations to the shallow water equations in spherical geometry, J. Comput. Phys. 102 (1992) 211–224.

[25] J. Galewsky, R. Scott, L. Polvani, An initial-value problem for testing numerical models of the global shallow-water equations, Tellus A: Dynamic Meteorology and Oceanography (56:5) (2004) 429–440.

[26] N. Feuillet, I. Manighetti, P. Tapponnier, E. Jacques, Arc parallel extension and localization of volcanic complexes in Guadeloupe, Lesser Antilles, J. Geophys. Res. 107 (2002) 3–1–3–29.

[27] R. J. LeVeque, K. Waagan, F. I. Gonzalez, D. Rim, G. Lin, Generating random earthquake events for probabilistic tsunami hazard assessment, In Global Tsunami Science: Past and Future, Birkhauser, Cham., 2016, pp. 3671–3692.

[28] F. Shi, J. T. Kirby, J. C. Harris, J. D. Geiman, S. T. Grilli, A high-order adaptive time-stepping tvd solver for boussinesq modeling of breaking waves and coastal inundation, Ocean Modelling 43-44 (2012) 36–51.

[29] H. Charnock, Wind stress on a water surface, Q. J. Roy Meteor Soc. (81) (1955) 639–640.

[30] H. Muller, L. Pineau-Guillou, D. Idier, F. Ardhuin, Atmospheric storm surge modeling methodology along the french (Atlantic and English Channel) coast, Ocean Dyn. (64(11)) (2014) 1671–1692.

[31] K. Knapp, M. Kruk, D. Levinson, H. Diamond, C. Neumann, The international best track archive for climate stewardship (IBTrACS): unifying tropical cyclone best track data., Bulletin of the American Meteor Society (91) (2010) 363–376.

[32] G. Holland, An analytic model of the wind and pressure profiles in hurricanes, Monthly Weather Review (108) (1980) 1212–1218.

[33] S. Saha, S. Moorthi, H. Pan, X. W. et al., The NCEP climate forecast system reanalysis, Bull. Am. Meteor. Soc. (91) (2010) 1015–1057.

[34] W. Pringle, J. Gonzalez, B. Joyce, J. Westerink, A. J. V. der Westhuysen, Baroclinic coupling improves depth-integrated modeling of coastal sea level variations around Puerto Rico and the U.S. Virgin Islands, Journal of Geophysical Research: Oceans.

[35] B. R. Joyce, J. Gonzalez, A. J. V. der Westhuysen, D. Yang, W. J. Pringle, J. Westerink, U.S. IOOS coastal and ocean modeling testbed: Hurricane-induced winds, waves, and surge for deep ocean, reef-fringed islands in the Caribbean., Journal of Geophysical Research: Oceans.

[36] R. Abgrall, M. Ricchiuto, High order methods for CFD, in: R. d. B. Erwin Stein, T. J. Hughes (Eds.), Encyclopedia of Computational Mechanics, Second Edition, John Wiley and Sons, 2017.